Materials
Advances

ROYAL SOCIETY
OF CHEMISTRY

REVIEW

View Article Online
View Journal

Check for updates

Cite this: DOI: 10.1039/d6ma00545d

Designing high-performance thermistor manganites: a review of charge transport, TCR enhancement, and materials engineering strategies

Youssef Moualhi * and Hedi Rahmouni

Received 18th April 2026,
Accepted 2nd June 2026

DOI: 10.1039/d6ma00545d

rsc.li/materials-advances

This work presents a comprehensive investigation of the electrical transport, temperature coefficient of resistance (TCR), and thermistor parameters of manganite perovskites, with particular emphasis on the roles of dopant nature, dopant concentration, annealing temperature, and A-site deficiency. The results reveal that charge transport is governed by Mott variable range hopping (Mott-VRH) at low temperatures and thermally activated small polaron hopping (SPH) at high temperatures, with well-defined crossovers through the intermediate Shklovskii–Efros variable range hopping (ES-VRH) regime associated with Coulomb-gap effects. A strong tunability of electrical behavior is achieved through compositional and processing control. The nature of A- and B-site dopants significantly modifies lattice distortion, Mn–O–Mn bond geometry, and carrier concentration, thereby controlling conductivity order and activation energy. The increase in dopant concentration alters the Mn^{3+}/Mn^{4+} ratio and shifts the metal–semiconductor transition, while annealing temperature governs grain connectivity and defect density, leading to substantial changes in transport mechanisms. A-site deficiency further enhances carrier mobility and induces notable modifications in both conductivity and transition temperatures. TCR analysis demonstrates both NTCR and PTCR behaviors, with exceptionally high NTCR values reaching $-35\%\cdot K^{-1}$. The thermistor parameters exhibit wide ranges, with activation energies of 47–290 meV, β values of 545–3366 K, and sensitivity coefficients of up to $-3.74\%\cdot K^{-1}$. A clear correlation between E_a, β, α, and TCR confirms the thermally activated nature of conduction and highlights the role of structural disorder and electron–phonon interactions. These findings establish manganites as highly tunable functional materials and promising candidates for thermistors, infrared sensors, and advanced electronic applications.

I Introduction

Over the past few years, it has been widely recognized that the electrical properties of numerous oxide compounds depend strongly on temperature.[1–3] Accordingly, understanding and controlling DC transport behavior of the oxide systems is crucial for various applications, particularly in solid-state electronics, magnetic sensors, and spintronics.[4–6] Among several oxide systems, manganite perovskites have attracted considerable attention as promising thermistor materials due to their high thermal sensitivity, tunable electrical conductivity, chemical stability, and wide operating temperature range.[7–12] In particular, negative temperature coefficient (NTC) manganite thermistors are highly desirable for temperature sensing, infrared detection, circuit protection, and temperature compensation technologies because their resistance strongly depends on temperature.[7–10] The performance of thermistor materials is generally evaluated using several important parameters, including the temperature coefficient of resistance (TCR), activation energy (E_a), thermistor constant (β), sensitivity coefficient (α), thermal stability, and reproducibility over wide temperature intervals.[7–12] Recent studies demonstrated that manganite systems could exhibit exceptionally high TCR values and adjustable thermistor responses through suitable compositional engineering and processing optimization.[7–12] Nevertheless, several important challenges remain unresolved, particularly the optimization of thermistor stability, the understanding of the correlation between charge transport mechanisms and thermistor performance, and the control of carrier localization, structural disorder, and grain boundary effects induced by the dopant concentration, annealing conditions, and A-site deficiency.[7–12] Therefore, a deeper understanding of

---

Laboratoire de Recherche Matériaux Avancés et Nanotechnologies (LRMAN), Institut Supérieur des Sciences Appliquées et de Technologie de Kasserine, Université de Kairouan, BP 471, 1200 Kasserine, Tunisia. E-mail: moualhiyoussef7@gmail.com

the interplay between transport mechanisms and thermistor parameters is essential for the design of high-performance manganite-based thermal sensing devices. In the 1950s, scientists and engineers began to investigate the steady state or DC conductivity of hopping electronic systems, beginning with the discovery of impurity hopping conduction in numerous compounds such as germanium and silicon.[13] For various mixed valence oxides like the perovskites, it has been reported that the charge carrier's motions depend mainly on the density of states at around the Fermi level, the disorder energy, and the distance between the metal transition cations.[1] In general, multiple transport mechanisms contribute to the electrical conductivity of perovskite structures in different temperature ranges.[14]

Accordingly, in some manganites, at elevated temperatures, the electrical conduction and the occurrence of a semiconductor behavior can be explained by the activation of the small polaron hopping (SPH) conduction mechanism between transition-metal ions.[14] At low temperatures, the transport characteristics of certain insulators and semiconducting materials may be governed by the variable range hopping (VRH) conduction mechanism between localized electronic states.[14–17] For the non-interacting charge carriers, Mott and Davis investigated the origin of the electrical conductivity variation at low temperatures and attributed it mainly to the effect of cationic disorder present in the material.[15–17] The model proposed by Mott and Davis is valid for a constant density of states near the Fermi level or for a slowly varying function of energy.[15–17] Subsequently, Shklovskii and Efros reported that, due to the long-range Coulomb interactions among localized electronic states, the density of states near the Fermi level tends toward zero, leading to the formation of a parabolic Coulomb gap.[18]

The Efros–Shklovskii (SE) hopping model is valid in the intermediate temperature range, depending on the scale of the gap. Both Mott's and Efros–Shklovskii models have been successfully applied to numerous perovskite systems. Over the past few years, the crossover between the Mott and SE-VRH hopping regimes as a function of temperature has been experimentally observed, particularly in several doped manganite compounds.[15–18] Recently, it has been reported that some materials exhibit a crossover from the Mott-VRH to SE-VRH conduction associated with a small Coulomb gap.[18] In this review, we present a comprehensive analysis of the temperature dependence of electrical conductivity in manganite perovskite systems, with particular emphasis on the underlying charge transport mechanisms, the nature of charge carriers, and their dynamical behavior. Unlike previous review articles that mainly discuss manganite physics, isolated hopping models, or oxide thermistor materials separately, the present review provides an integrated and application-oriented perspective that correlates transport mechanisms, thermistor parameters, and compositional/and processing effects within a unified framework. Special attention is given to the interplay between variable range hopping (VRH), Shklovskii–Efros VRH, and small polaron hopping processes, which govern the electrical response over a wide temperature range. In addition, the temperature coefficient of resistance (TCR) and its associated parameters are systematically discussed to highlight their role in evaluating the thermal sensitivity of these materials. Particular emphasis is placed on the crossover between Mott-VRH, SE-VRH, and SPH conduction regimes and their relation to carrier localization and electron–phonon interactions. The thermistor-related parameters, including activation energy (E_a), thermistor constant (β), and sensitivity coefficient (α), are also analyzed as key descriptors of the transport properties. Furthermore, we critically examine the influence of intrinsic and extrinsic factors such as dopant nature, dopant concentration, A-site deficiency, and annealing temperature on the electrical conductivity, TCR behavior, and thermistor performance of manganite systems. These parameters are shown to play a crucial role in governing the metal–semiconductor transition, carrier localization, and overall conduction mechanisms through their impact on lattice distortion, Mn–O–Mn bond geometry, and carrier concentration. Another important contribution of this review is the establishment of direct correlations between electrical transport parameters and thermistor performance indicators, which provides deeper insight into the optimization of manganites for temperature-sensitive electronic applications. This review aims to provide microscopic insights into charge transport phenomena in oxide perovskites and to establish clear structure–property correlations that are essential for optimizing their functional performance. Finally, the collected results highlight the strong potential of engineered manganite systems for advanced functional applications, particularly in thermistors, infrared sensors, and temperature-sensitive electronic devices.

II Discussion

For ceramic compounds, both the nearest-neighbour hopping and variable-range hopping (VRH) conductivity mechanisms have been proposed to explain the origin of the conductivity increase in perovskite systems.[15–17] The point is that, in perovskite materials, the probability of finding an empty nearest site with an energetically favorable localized state for electron hopping decreases rapidly with decreasing temperature.[1] Therefore, the semiconducting behavior of these materials results from the competition between two conduction mechanisms, namely hopping between nearest sites with large energy differences and hopping between sites beyond nearest neighbors with smaller energy differences. With decreasing temperature, particularly in the low-temperature region ($T < \theta_D/4$), several systems exhibiting localized charge carriers show a crossover from the Mott variable range hopping (Mott-VRH) conduction mechanism to the Shklovskii–Efros variable range hopping (SE-VRH) process.[1] Fig. 1(a) and (b) illustrate schematic representations of the temperature dependence of the electrical conductivity for manganite systems exhibiting metallic, semiconductor (SC), and metal–semiconductor transition behaviors. In Fig. 1(a), the blue curve represents a metallic behavior, where the electrical conductivity decreases with increasing temperature due to strong delocalized cation–cation interactions and enhanced carrier scattering effects.[19] The pink

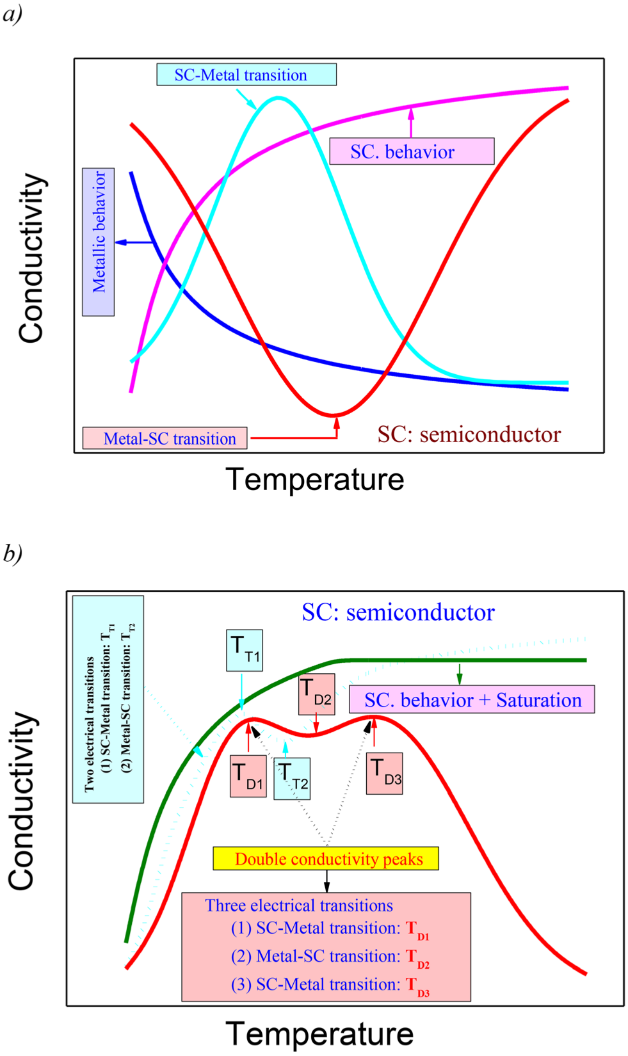

Fig. 1 Possible evolutions of the electrical conductivity as a function of temperature for the manganite oxide systems.

curve corresponds to a typical semiconductor behavior, in which the conductivity increases with temperature because of thermally activated hopping transport mechanisms. The cyan curve illustrates a semiconductor-to-metal (SC–metal) transition, reflecting a crossover from localized charge transport to delocalized carrier conduction induced by strong double-exchange interactions. In contrast, the red curve indicates a metal-to-semiconductor (metal–SC) transition, where the conductivity reaches a minimum value before increasing again at elevated temperatures due to the activation of localized hopping mechanisms. Fig. 1(b) presents more complex transport behaviors involving multiple electrical transitions and conductivity saturation effects. The green curve corresponds to a semiconductor behavior followed by conductivity saturation at elevated temperatures. The dotted cyan curve exhibits two distinct electrical transitions: a semiconductor-to-metal transition at T_{T1} followed by a metal-to-semiconductor transition at T_{T2} before ultimately leveling into a semiconductor behavior. The red curve illustrates systems showing double conductivity peaks and three successive electrical transitions: semiconductor-to-metal (T_{D1}), metal-to-semiconductor (T_{D2}), and semiconductor-to-metal (T_{D3}). These transitions arise from the competition between localized hopping conduction mechanisms and delocalized double-exchange interactions. Accordingly, the semiconductor regions are generally governed by localized transport processes such as Mott-VRH, SE-VRH, or SPH conduction, whereas the metallic regions are associated with carrier delocalization caused by strong cation–cation interactions.[19] This variation has recently been reported in the $La_{0.7}Sr_{0.25}Na_{0.05}Mn_{0.7}Ti_{0.3}O_3$ perovskite system.[20] A second type of transition from metallic to semiconducting behavior has been observed in various perovskites such as the $Sm_{0.45}Pr_{0.10}Sr_{0.45}MnO_3$ manganite.[21] In this case, the electrical conductivity decreases with increasing temperature, reaching a minimum value at a characteristic transition temperature T_{M-S}, and then starts to increase after that, indicating the onset of semiconducting behavior in the material. For the mentioned system, the authors have attributed the occurrence of semiconducting behavior, beyond T_{M-S}, to the activation of two distinct conduction processes (the SPH process at high temperatures and the SE-VRH process in the intermediate temperature range). At low temperatures, the metallic behavior of the $Sm_{0.45}Pr_{0.10}Sr_{0.45}MnO_3$ system is generally attributed to the presence of various scattering processes. In the literature, it has been reported that a single conduction model is insufficient to fully explain the origin of the electrical transport properties and the dynamics of the charge carriers in manganite oxides over a wide temperature range. Therefore, various conduction models have been employed to adequately explain the origin of the electrical conductivity variation in these materials.[1] Explicitly, numerous hopping and scattering processes have been reported in the literature to understand the origin of the metallic and semiconducting behaviors of perovskite systems. For materials exhibiting semiconducting behavior, the electrical conductivity increases continually with increasing temperature. In this case, no strong cation–cation interactions are observed in the material. Therefore, the cation–anion–cation interactions govern the transport phenomena and attenuate the cation–cation interactions.[19] In the literature, these types of interactions are generally explained by the hopping motions of charge carriers between localized states. Accordingly, for temperatures higher than $\theta_D/2$ (where θ_D is the Debye temperature characteristic of each material), the occurrence of cation–anion–cation interactions leads to the formation of localized electrons (polarons), which move between the neighboring states to enhance the conductivity behavior and indicate the emergence of semiconducting behavior in the materials. For temperatures below $\theta_D/2$, different hopping regimes may become active depending on the considered temperature interval. In the low-temperature region ($T < \theta_D/4$), the semiconducting behavior is generally described by the Mott-VRH model,[16] which explains the conductivity variation through the hopping motion of electrons between localized states with the variable range distances.

In the intermediate temperature range ($\theta_D/4 \leq T \leq \theta_D/2$), the Coulomb interaction between localized charge carriers becomes significant, leading to the activation of the

Shklovskii–Efros VRH (SE-VRH) mechanism. In this context, the variation in electrical conductivity and the occurrence of semiconducting behavior in oxide materials can generally be explained on the basis of the SPH and/or the VRH processes. According to previous experimental and theoretical works,[1,20] the identification of the nature and the number of activated conduction processes can be achieved through the investigation of the evolution of electrical conductivity as a function of the inverse of temperature (Fig. 2(a)). At elevated temperatures, the activation of the SPH conduction process is principally identified using the plot of ln($\sigma_{dc}\cdot T$) *versus* $1/T$. The presence of this type of process can be confirmed by the linear behavior of the curve in the high temperature region. Such linearity is also widely employed in the literature to determine the hopping, binding, and disorder energies of the materials over a wide temperature range. Mainly, the characteristic temperature $\theta_D/2$ is experimentally estimated from the deviation of the linear behavior in the ln($\sigma_{dc}.T$) *versus* $1/T$ plots at elevated temperatures. This deviation indicates the progressive breakdown of the SPH linear regime and marks the transition between thermally activated small polaron hopping and low-temperature hopping conduction mechanisms. Following previous theoretical and experimental investigations on manganite systems, the corresponding temperature is associated with approximately half of the Debye temperature ($\theta_D/2$).[1,6,13–16] Consequently, the low-temperature transport region below $\theta_D/2$ is analyzed within the VRH framework. Additionally, in Anderson localized systems, the VRH conduction mechanism is a very general process below half of the Debye temperatures. More specifically, the Mott-VRH mechanism is generally dominant at low temperatures ($T < \theta_D/4$), while the SE-VRH regime becomes active at intermediate temperatures due to the formation of a Coulomb gap near the Fermi level. It should be noted that the $\theta_D/4$ and $\theta_D/2$ boundaries correspond to approximate characteristic temperature ranges commonly used in the literature rather than strict universal limits, since their exact values may depend on the composition, lattice disorder, and electron–phonon interaction strength of the investigated manganite compounds.[1,6,13–16] According to the Mott model, the VRH conductivity can be obtained by optimizing (minimizing) the η exponent, which is given by the following relation:[15–17]

$$\eta = \frac{2r}{\xi} + \frac{E_a}{k_B T}$$

Within the framework of the VRH model, the following relation correlates the hopping probability with the exponent defined above:[15–17]

$$p = p_0 \exp(-\eta)$$

Factor ξ is the localization length, E_a is the hopping energy, and r denotes the hopping distance. The aforementioned parameters

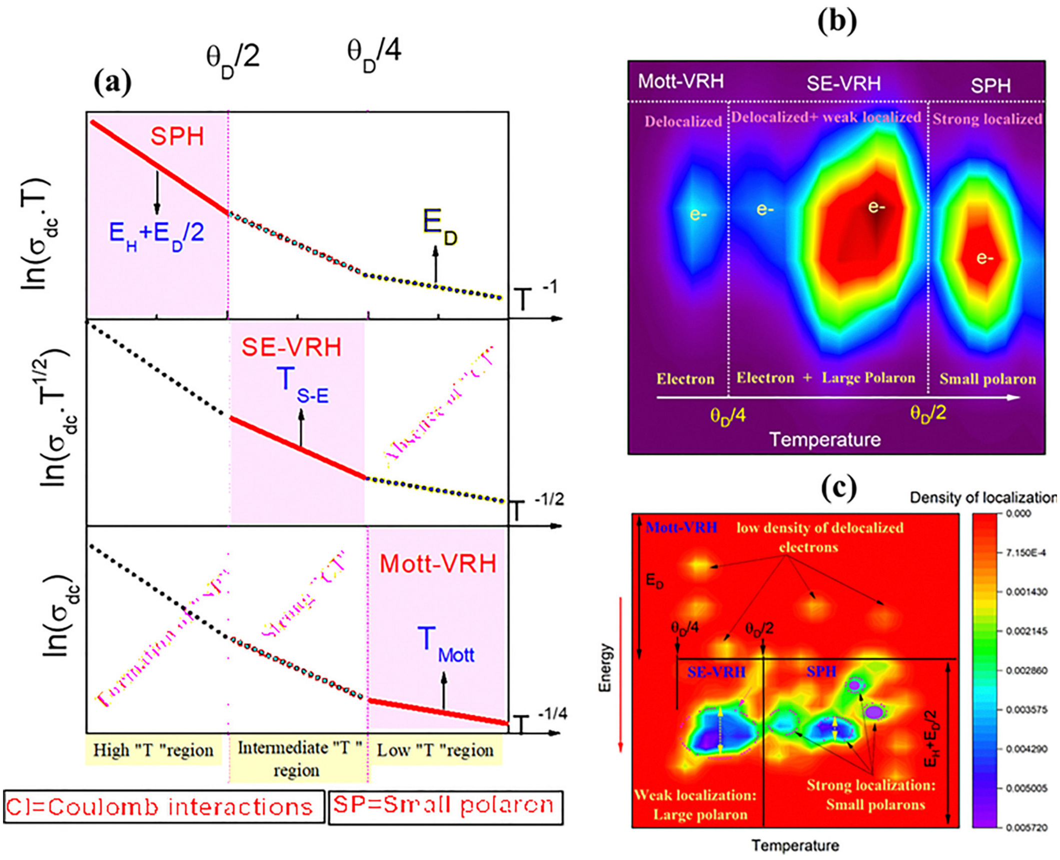

Fig. 2 Conduction mechanisms defining the semiconductor behavior of the perovskites in the DC regime (a). Various kinds of charge carriers defining the electrical conductivity of the manganite oxides (b and c).

are interrelated through the three-dimensional normalization relation, which describes the one-particle density of states $g(\varepsilon)$:

$$\frac{4}{3}\pi r^3\int_0^{\varepsilon} g(\varepsilon)\mathrm{d}\varepsilon = 1$$

Parameter ε represents the one-particle energy. At low temperatures, oxide materials are generally characterized by a reduced phonon density and lower phonon energy. In this case, the energy difference between two adjacent sites becomes too large for the nearest neighbor hopping process to persist. Consequently, the charge carriers tend to hop towards more energetically favorable sites. This conduction mechanism is referred to as VRH. As pointed out by Mott, the conduction sites in the limit of the VRH regime are assumed to be identical.[15–17] In addition, the conduction phenomena occur within the gap region and around the Fermi level. At low temperatures, the Coulomb interactions between the charge carriers are neglected within the Mott-VRH approximation. Since the density of states near the Fermi level is assumed to be constant, the derivation of the aforementioned optimization condition leads to the three-dimensional Mott-VRH model for the electrical conductivity and its temperature dependence:[15–17]

$$\sigma_{\mathrm{dc}}(T) = \sigma_0 \exp\left(\frac{-T_{\mathrm{M}}}{T}\right)^{1/4}$$

Mainly, the evolution of pre-exponential factor σ_0 with temperature is weak in comparison with the exponential term. For this reason, its temperature dependence is generally neglected. T_{M} is the characteristic Mott temperature, which is related to ξ and $N(E_{\mathrm{F}})$ through the following relation:[15–17]

$$T_{\mathrm{M}} = \frac{\beta_{\mathrm{M}}}{k_{\mathrm{B}}\xi^3 N(E_{\mathrm{F}})}$$

The β_{M} factor is a coefficient parameter. In the literature, the Mott-VRH model has been more thoroughly confirmed by Pollak.[22] Nevertheless, there is a significant inconsistency in the values of the β_{M} coefficient. In the intermediate temperature domains ($\theta_{\mathrm{D}}/4 \leq T \leq \theta_{\mathrm{D}}/2$), the occurrence of semiconducting behavior in perovskite structures is generally analyzed using the SE-VRH model.[18] For temperatures higher than $\theta_{\mathrm{D}}/2$, the transport mechanism progressively changes toward thermally activated small polaron hopping (SPH) due to enhanced electron–phonon interaction and lattice distortion effects. Fig. 2(b and c) illustrates the evolution of the charge carrier nature and the conduction process as a function of the temperature. It should be noted that these panels are schematic representations based on the transport models (Mott-VRH, SE-VRH, and SPH), rather than experimental electron density maps. From Fig. 2(b and c), it can be found that the conduction mechanism evolves upon heating from Mott-VRH ($T < \theta_{\mathrm{D}}/4$) to SE-VRH ($\theta_{\mathrm{D}}/4 \leq T \leq \theta_{\mathrm{D}}/2$) and finally to the SPH regime for $T > \theta_{\mathrm{D}}/2$ and is controlled by the charge carrier nature and density. Accordingly, the appearance of the low density of electrons at low temperatures favors the hopping motion of those charges to variable ranges *via* a disordered energy E_{D}. In the intermediate temperature regions, the mentioned crossover is mainly related to the increase in the density of the charge carriers and the weak localization of the electrons. The latter favors the formation of large polarons. Thus, the SE-VRH regime can be considered as a transition region between strongly localized carriers in the Mott-VRH regime and thermally activated small polarons at elevated temperatures. At high temperatures, small polarons can arise due to the interaction between electrons and phonons. Accordingly, polaron formation typically occurs when an electron interacts with the lattice, causing a localized distortion in the crystal structure. This distortion creates a region of local charge redistribution (lattice polarization), where the electron and its surrounding lattice deformation together behave as a single entity. The presence of polarons can significantly influence the electrical conductivity behavior of manganite perovskite oxides. After the formation of small polarons at elevated temperatures, charge carriers become localized due to the strong electron–phonon interaction and lattice distortion. Electrical conduction then occurs *via* thermally activated hopping of these small polarons between neighboring sites, which leads to an increase in electrical conductivity with temperature.

III Experimental validation

III.A Morphological evolution and defect engineering in polycrystalline manganites

Fig. 3 schematically summarizes the ideal and distorted structural features of substituted perovskite manganites with the general formula ABO_3. Fig. 3(a) presents the three-dimensional pseudo-cubic crystal structure composed of corner-sharing MnO_6 octahedra, where the A-site cations (rare-earth or alkali-earth ions) occupy the dodecahedral cavities and the B-site Mn ions are located at the octahedral centers. The chemical substitution mechanisms are illustrated in Fig. 3(b), including both A-site substitution through alkaline-earth or alkali-metal doping and B-site substitution *via* transition-metal incorporation. Fig. 3(c) highlights the formation of structural point defects, particularly A-site and B-site cation vacancies, which locally disrupt lattice symmetry and modify the electronic environment. The structural consequences of these substitutions and defects are further illustrated in Fig. 3(d), where an ideal MnO_6 octahedron is contrasted with a distorted octahedron resulting from Jahn–Teller effects or the ionic size mismatch. Finally, Fig. 3(e) depicts the cooperative tilting of corner-sharing octahedra induced by internal lattice strain, transforming the ideal Mn–O–Mn bond angle from 180° to a distorted configuration below 180°. Such steric distortions strongly affect the overlap between Mn d-orbitals and O p-orbitals, thereby modulating the double-exchange interaction, electronic transport, and magnetotransport properties of manganite materials. A comprehensive understanding of the physical behavior of polycrystalline manganites requires a multiscale investigation of their morphology, extending from the macroscopic grain arrangement to the atomic-scale lattice structure. Fig. 4 schematically illustrates the hierarchical structural and defect characterization of polycrystalline manganites

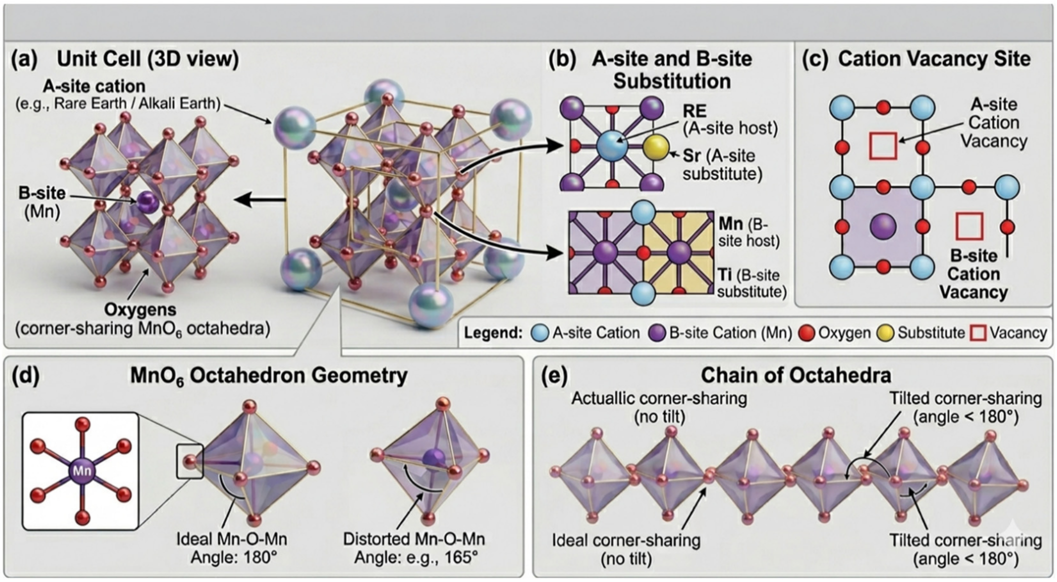

Fig. 3 Schematic illustration of the ABO_3 perovskite unit cell, showing A-/B-site substitution, cation vacancies, and MnO_6 octahedral tilt distortions.

across different spatial scales using complementary electron microscopy techniques. At the micrometer scale, scanning electron microscopy (SEM) reveals the surface morphology and grain organization, highlighting the presence of interconnected grains, grain boundaries, pores, and micro-cracks generated during processing. Statistical analysis of SEM images provides quantitative information of the grain size and grain size distribution, parameters that critically influence the electrical conductivity, magnetic exchange interactions, and mechanical stability of ceramic manganites. At smaller length scales, transmission electron microscopy (TEM) provides insight into the internal nanostructure of the grains, frequently revealing that larger grains are themselves composed of nanoscale crystallites separated by well-defined interfaces. Furthermore, high-resolution TEM (HRTEM) enables direct visualization of lattice fringes and atomic ordering, allowing the identification of structural defects such as dislocations, stacking faults, strain fields, and localized point defects including cation and oxygen vacancies. Fig. 4 therefore demonstrates the progressive transition from the grain-scale morphology to atomic-scale defect mapping and emphasizes how these structural characteristics collectively govern the functional properties of manganite oxides. In the present work, the morphology of manganites is discussed through two representative mechanisms of microstructural tuning: the effect of annealing temperature and the effect of A-site cation deficiency. The influence of annealing temperature on the microstructural evolution of the $La_{0.9}Sr_{0.1}MnO_3$ manganite system is illustrated in the bright-field TEM micrographs shown in Fig. 5(a–d). A pronounced temperature-driven transformation in grain morphology, grain size, and grain-boundary structure is observed. At low annealing temperatures, the material remains in a nanostructured regime. As shown in Fig. 5(a), the sample annealed at 600 °C exhibits heavily agglomerated and irregular nanoparticles with the average grain diameter centered around 56.8 nm. The increase in the annealing temperature to 800 °C (Fig. 5(b)) shifts the grain size distribution toward a larger average value of approximately 80.9 nm, accompanied by visible neck formation between adjacent particles, characteristic of the initial stage of solid-state sintering driven by surface-energy minimization. A more pronounced structural transformation occurs at higher annealing temperatures. At 1000 °C (Fig. 5(c)), the system enters an intermediate sintering regime characterized by rapid grain coarsening and the formation of dense, faceted grains with an average size of approximately 229.4 nm. This grain growth process is mainly governed by grain-boundary migration and localized Ostwald ripening, where larger crystallites grow at the expense of smaller high-energy particles. Upon further increasing the annealing temperature to 1200 °C (Fig. 5(d)), the material undergoes nearly complete sintering and evolves into a micrometric regime with an average grain size of about 863.5 nm. The highly disordered grain boundaries observed at lower temperatures are progressively replaced by large monolithic crystallites exhibiting sharp geometric facets and significantly reduced porosity. This thermal evolution demonstrates that annealing temperature constitutes an efficient route for tailoring grain-boundary density and connectivity, which are expected to strongly affect grain-boundary magnetoresistance and magnetic domain-wall dynamics in mixed-valence manganites. The effect of A-site cation deficiency on the surface morphology and microstructural evolution of the $La_{0.8}Na_{0.2-x}\square_xMnO_3$ ($x = 0.00$, 0.05, 0.10, and 0.15) manganite system was investigated using SEM, and the corresponding grain size distributions are presented in Fig. 6(a–d). The stoichiometric sample ($x = 0.00$) exhibits a highly heterogeneous polycrystalline microstructure composed of strongly agglomerated and irregularly shaped grains with pronounced faceting, resulting in a broad and right-skewed grain size distribution extending beyond 10 μm. As the Na deficiency increases, a progressive and systematic modification of the microstructure is observed. The morphology evolves from

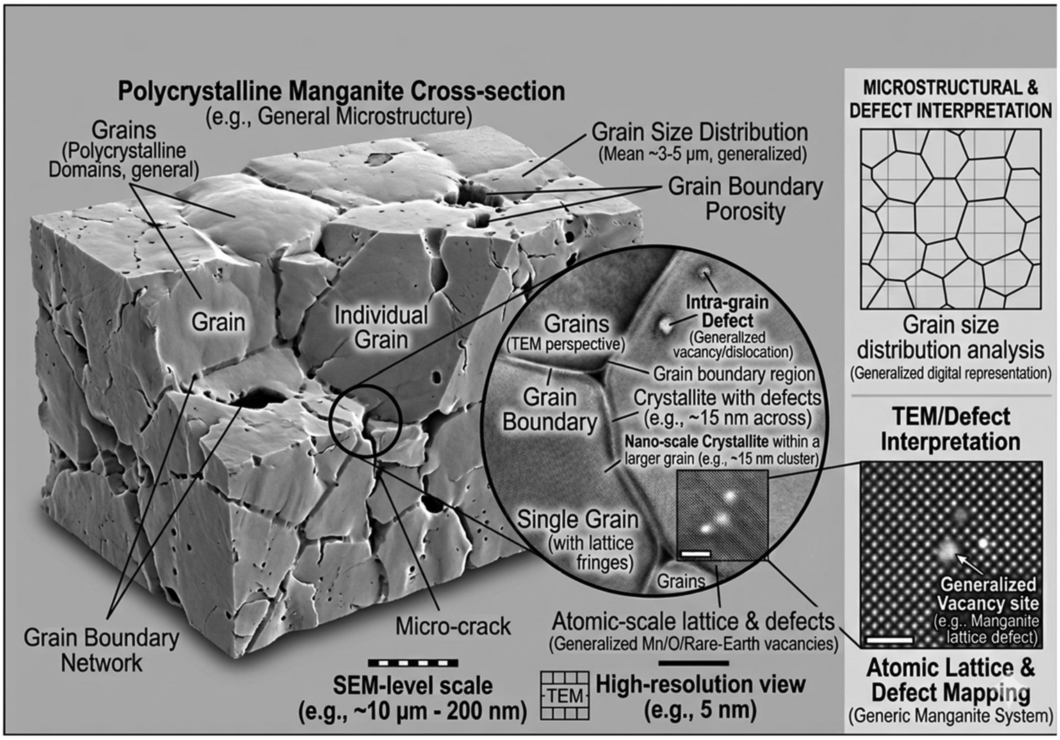

Fig. 4 Hierarchical morphological and defect fingerprinting in poly-crystalline manganite.

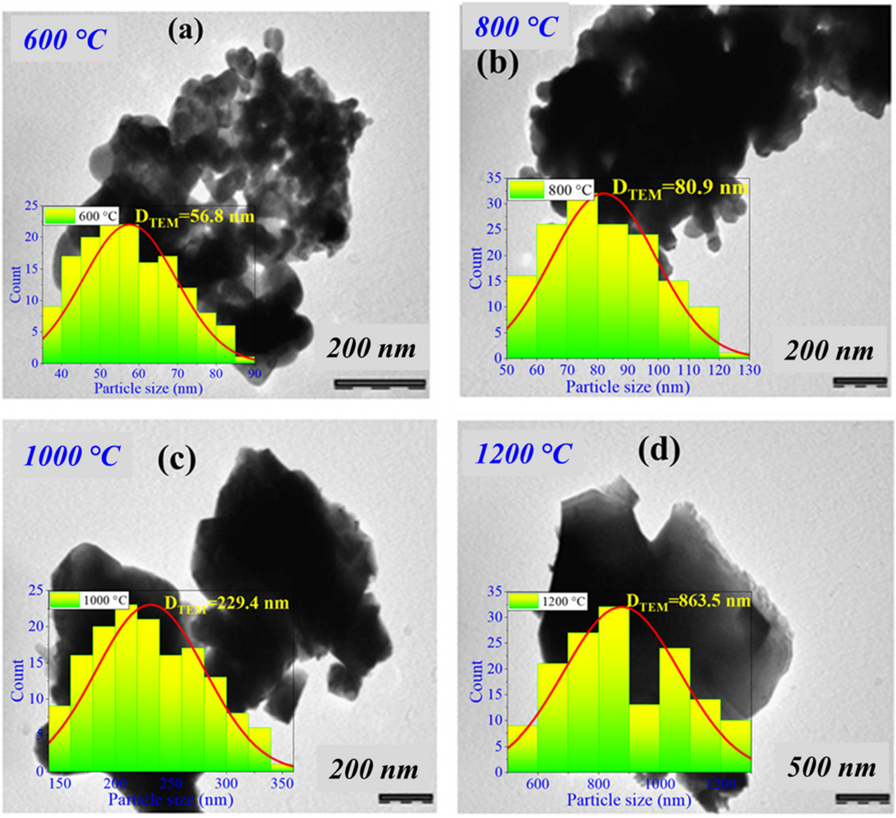

Fig. 5 Bright-field transmission electron microscopy (TEM) micrographs of $La_{0.9}Sr_{0.1}MnO_3$ manganites annealed at different temperatures: (a) 600 °C, showing highly agglomerated initial nanoparticles; (b) 800 °C, demonstrating the onset of grain necking; (c) 1000 °C, illustrating rapid grain coarsening and facet development; and (d) 1200 °C, showing complete recrystallization into massive, monolithic micro-grains.

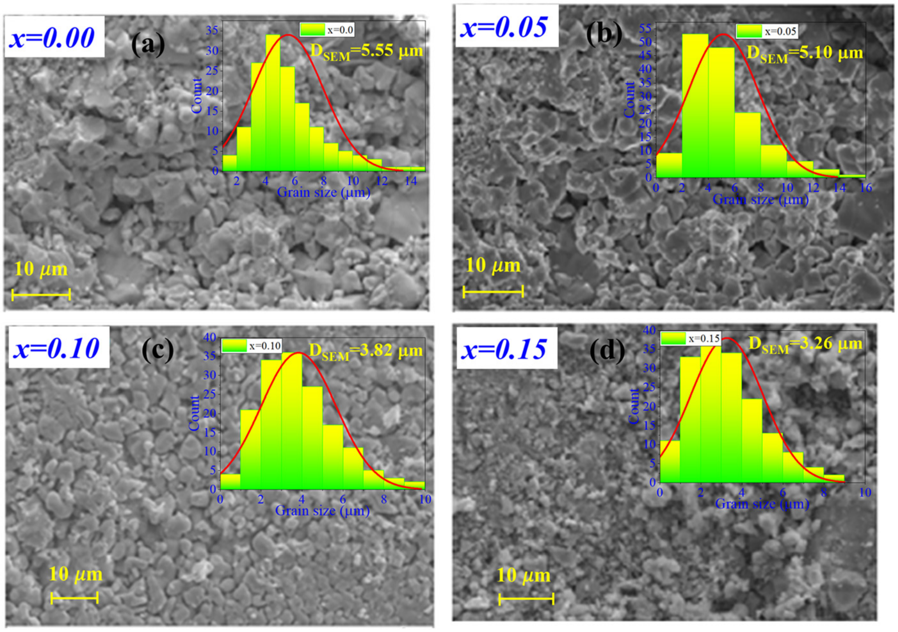

Fig. 6 Surface morphology and grain size analysis of $La_{0.8}Na_{0.2-x}\square_xMnO_3$ manganites with varying defect concentrations (x).

large consolidated grains toward a more homogeneous distribution of rounded and isolated particles. Simultaneously, the grain size distributions become narrower and shift toward smaller dimensions, changing from a coarse-grained regime centered around 5.55 µm for $x = 0.00$ to a predominantly fine-grained and sub-micrometric regime (3.26 µm) for $x = 0.15$. This reduction in grain size with increasing Na deficiency can be attributed to the suppression of grain-boundary mobility during the sintering process. The introduction of nominal A-site vacancies (□) through Na deficiency reduces the diffusion kinetics required for grain growth. In addition, these vacancy-related defects and local compositional fluctuations may induce a solute-drag effect or segregate preferentially at grain boundaries, thereby pinning the boundaries and inhibiting grain coalescence. Consequently, A-site deficiency acts as an effective microstructural control parameter, enabling a direct transition from a coarse and highly agglomerated ceramic matrix to a refined fine-grained morphology. Collectively, the results obtained from both annealing-temperature variation and A-site defect engineering demonstrate the strong sensitivity of the manganite microstructure to processing conditions and defect chemistry, confirming the critical role of the morphology in determining the functional properties of perovskite manganites.

III.B Impact of the nature of the doping element on the electrical conductivity behavior

Based on previously reported investigations, it has been observed that the nature of the doped element in both A and B sites of the ABO_3 perovskite structure affects mainly the dynamics of the charge carriers, the conductivity/resistivity value, and the material electrical behavior.[23,24] Accordingly, it has been shown that modifying the dopant nature mainly affects the electrical resistivity order. Such kinds of effects are primarily attributed to the variation in the ionic radius that, in turn, control hopping processes and the cations' interactions through the materials. In this context, it is found that the nature of the doping element affects principally the lattice distortion force that is related to its ionic radius. On the one hand, in the case of manganites, the variation in the ionic radius affects the crystal structure and the lattice parameters of the compound. For lanthanum manganites, smaller or larger dopants compared to the La ion can cause lattice strain, leading to changes in the Mn–O bond length and Mn–O–Mn bond angle, which directly affect the charge carriers hopping mechanisms.[25] On the other hand, the nature of the doping element controls the valence state and the carrier concentration in manganites. Dopants such as Sr^{2+}, Ca^{2+}, Ba^{2+}, and Pb^{2+} partially substitute the trivalent Pr^{3+} or La^{3+} ions, thereby introducing holes into the system and leading to the coexistence of Mn^{3+} and Mn^{4+} mixed-valence states. In such materials, it has been reported that the increase in the Mn^{4+} ion concentration mainly enhances the double-exchange interactions that govern the electrical phenomena in oxide compounds. Since the nature of the dopant element controls the charge carrier concentration, the effect of doping on electrical conductivity depends strongly on the specific manganite system and the type of dopant introduced. In several manganites, divalent dopants such as Sr^{2+} or Ca^{2+} can enhance the Mn^{3+}/Mn^{4+} double-exchange interaction and improve the electrical conductivity. However, in some cases, dopants such as Pr or Nd may induce structural distortion and charge localization, resulting in a reduction of electrical conductivity. For the $La_{0.7}Ca_{0.3}MnO_3$ manganite, Li *et al.*[25] investigated the substitution of Ca cations with three different elements (Pb, Sr, and Ba). Their study demonstrated that variations in the

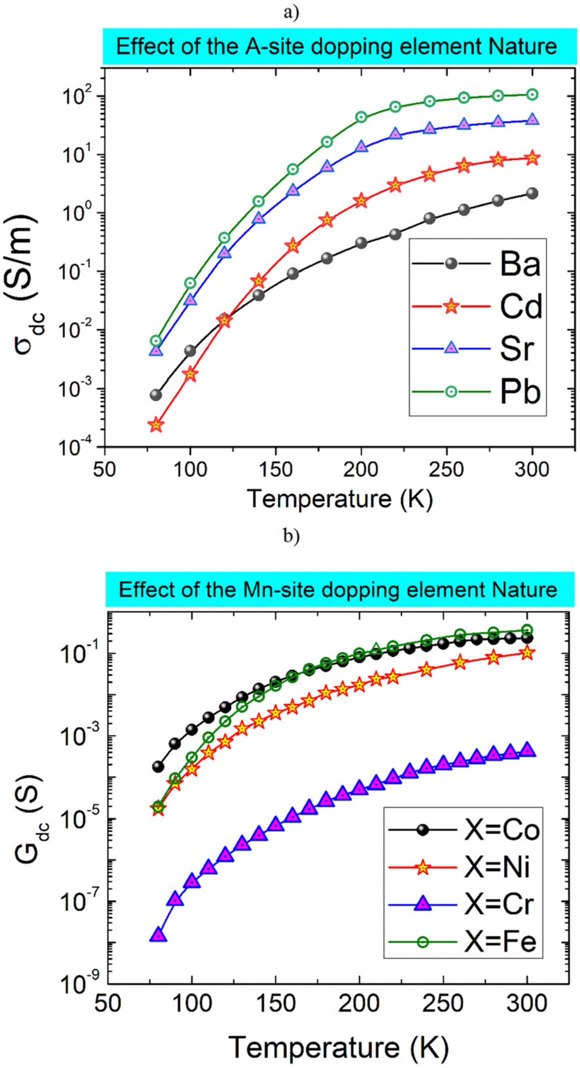

Fig. 7 Temperature dependence of the electrical dc-conductivity for two different manganite structures: the impact of the nature of the doping element on the A site $Pr_{0.65}Ca_{0.25}X_{0.1}MnO_3$ (X = Ba, Cd, Sr and Pb) (a) ref. 26 and the B-site $Pr_{0.7}Ca_{0.3}Mn_{0.9}X_{0.1}O_3$ (X = Co, Ni, Fe, and Cr) (b) ref. 27. Panel (a) adapted from ref. 26 with permission from Elsevier, copyright 2020. Panel (b) adapted from ref. 27 with permission from the Royal Society of Chemistry, copyright 2020.

average ionic radius at the A-site lead to an increase in the Mn–O–Mn bond angle. This structural modification influences the strength of the double-exchange interaction, which primarily governs the charge-carrier dynamics in manganite oxides. In particular, Ba substitution was found to significantly increase the electrical resistivity of the material. Furthermore, Li *et al.*[25] reported that the nature of the dopant element strongly affects the temperature coefficient of resistance (TCR), a key parameter for achieving high-performance thermistor ceramic systems. Beyond composition-specific observations, the reported studies collectively indicate that the electrical transport behavior of manganites follows common structural-electronic correlations, where the balance between double-exchange interactions, lattice distortion, and charge-carrier localization determines the final conductivity and thermistor response. In general, dopants inducing strong lattice distortion favor carrier localization and enhanced semiconducting behavior, whereas dopants increasing the electronic bandwidth tend to improve metallic conduction and electrical conductivity.

Fig. 7(a) shows the evolution of the electrical conductivity *versus* the temperature for the $Pr_{0.65}Ca_{0.25}X_{0.10}MnO_3$ (X = Ba, Sr, Cd, and Pb) system.[26] The reported results show that the electrical conductivity increases with increasing temperature, which is the normal behavior of the semiconducting materials. In the literature, the occurrence of a semiconductor behavior is mainly related to the increase in the density of the charge carriers and their mobility.[1,27] For all the studied samples, we found that the electrical conductivity depends mainly on the nature of the dopant element at the A site in $AMnO_3$ manganites. A similar dependence of the electrical conductivity order on the nature of the dopant element has been observed in other manganites like $La_{0.7}Ca_{0.3-x}Pb_xMnO_3$ (x = 0.0 and 0.1) and $La_{0.7}Ca_{0.3-x}Sr_xMnO_3$ (x = 0.0 and 0.1). As compared with the $La_{0.7}Ca_{0.3}MnO_3$ manganite, Phong *et al.*,[28] Cao *et al.*,[29] and Li *et al.*[25] found that replacing Ca with Pb or Sr increases the average ionic radius of the manganites. This modification, in turn, affects the cationic disorder, which increases from σ^2 ($La_{0.7}Ca_{0.3}MnO_3$) = 3.3600 × 10^4 (Å^2) to σ^2 ($La_{0.7}Ca_{0.2}Pb_{0.1}MnO_3$) = 19.850 × 10^4 (Å^2) upon Pb substitution at the Ca site. In the same context, this substitution process mainly modifies the Mn–O–Mn bond angles and the Mn–O bond distances. These factors are among the principal parameters governing the ionic interactions between Mn cations. In this case, we can assume that changing the nature of the dopant element can modify the density of the charge carriers and their mobility, which are considered among the principal factors for controlling the electrical conductivity order and the electrical behavior of the material. Fig. 7(b) shows the temperature dependence of the electrical conductance for $Pr_{0.7}Ca_{0.3}Mn_{0.90}X_{0.10}O_3$ (X = Ni, Co, Cr, and Fe) perovskites.[27] The plotted results indicate that all the studied manganites exhibit semiconducting behavior over the explored temperature range, as confirmed by the increase in electrical conductance with increasing temperature for all samples. Therefore, the nature of the dopant element does not alter the overall electrical behavior of the material. However, it significantly influences the mobility and density of the charge carriers. From the same results, the plotted curves indicate that the studied temperature domain can be divided into two main regions. At low temperatures, the electrical conductivity and transport properties are mainly governed by the effect of cationic disorder in the manganite compounds. In the present study, our results are in good agreement with Mott's theory.[15–17] Accordingly, we found that changing the nature of the dopant element mainly affects the material's conductivity ordering, especially at low temperatures. The observed behavior can be attributed to the difference between the ionic radii of the Mn cation and the Ni, Co, and Cr elements. Likewise, it thereby became evident that the electrical properties of the materials change mainly at high temperatures when we modify the nature of the doping element. These results suggest that the nature of the dopant element influences the activation energy values. This behavior can be attributed to modifications in the polaron hopping mechanism, since the activation energy is closely related to both polaron formation and charge-carrier hopping between neighboring Mn sites in manganite compounds. Therefore, modifying the B site cationic disorder can also be considered as an effective route to tune the dynamics of the charge carriers, in agreement with previous reports in manganite systems.[7,30–32] This approach offers a potential strategy for designing materials with tailored electrical properties for future applications.

III.C Impact of the concentration of the doping element on the electrical conductivity variation

According to several previous investigations,[32–35] it has been reported that the increase in the dopant concentration significantly modifies the electrical properties of the materials. Such modifications are also accompanied by changes in the crystallographic parameters of the material. By increasing the substitution level in the A or Mn sites, it is possible to modify the Mn–O–Mn bond angle and the Mn–O distances.[32–35] The aforementioned parameters are among the most common factors defining the physical properties of manganite oxide materials. In addition, previous studies[32–35] have consistently reported that the increase in the substitution concentration leads to a significant modification of the Mn^{3+}/Mn^{4+} ratio, which plays a crucial role in determining the electrical and magnetic properties of manganite materials. This governs the metal-semiconductor transition temperature, the density of free charge carriers, the number of available paths for the conduction phenomena, and the activation energy for the transfer of charge carriers *via* the SPH and VRH processes. These hypotheses are in good agreement with the reported experimental results in the present work. Accordingly, we found from our results that the increase in the substitution level affects the metal-semiconductor transition temperature and the conductivity values of both the Pr doped A-site of $Sm_{0.55-x}Pr_xSr_{0.45}MnO_3$ (x = 0.0, 0.1, and 0.2)[36] and the Al-doped Mn-site of $La_{0.6}Sm_{0.1}Ba_{0.33}Mn_{1-x}Al_xO_3$ (x = 0.0, 0.05, 0.1, 0.15, and, 0.2) systems (Fig. 8(a and b)). Consequently, we found from Fig. 8(a) that the increase in the Pr concentration increases the metal–semiconductor transition temperature from T_{M-S} = 120 K for x = 0.0 to T_{M-S} = 180 K for x = 0.2 and favors enhanced metallic behavior in the material. Moreover, the reported result in Fig. 8(a) indicates that the increase in the Pr concentration improves the conductivity, especially at low temperatures. This behavior can be attributed to structural distortions induced by the ionic radius mismatch between Sm^{3+} and Pr^{3+}, which modifies the Mn–O–Mn bond angle and the electronic bandwidth, thereby influencing the double-exchange interaction and shifting the metal–semiconductor transition toward higher temperatures. Consequently, the temperature range of metallic-like conduction is extended with increasing Pr content. In the same context, the obtained results in Fig. 8(a) can be attributed to the large mismatch between the cationic radius of the Sm and the Pr elements, which induces structural distortions in the MnO_6 network and modifies the Mn–O–Mn bond geometry, thereby affecting carrier mobility. This interpretation is consistent with the Mott variable range hopping framework[13,15–17] and related transport models commonly used for disordered manganites. Although the ionic radii of Sm^{3+} and Pr^{3+} are different, both ions possess the same valence state (+3). Therefore, the substitution process preserves the overall charge neutrality of the compound and does not significantly affect the Mn^{3+}/Mn^{4+} ratio. In this case, the substitution process does not affect the Mn^{3+}/Mn^{4+} ratio in the compound. However, it strongly modifies the Mn–O bond length and the Mn–O–Mn bond angles. For the $La_{0.6}Sm_{0.1}Ba_{0.33}Mn_{1-x}Al_xO_3$ (x = 0.0, 0.05, 0.1, 0.15, and, 0.2) system, the reported results in Fig. 8(b) indicate that the increase in the Al concentration in the Mn site is accompanied by a shift of the metal-semiconductor transition toward lower temperatures. For x = 0.2, we found that the material exhibits a semiconducting behavior over the entire explored temperature range. In this case, substituting the manganite system with other transition elements directly modifies the Mn^{3+}/Mn^{4+} ratio, the Mn–O bond length, and the Mn–O–Mn angles. This mainly affects the electrical conductivity values, which decrease by more than two

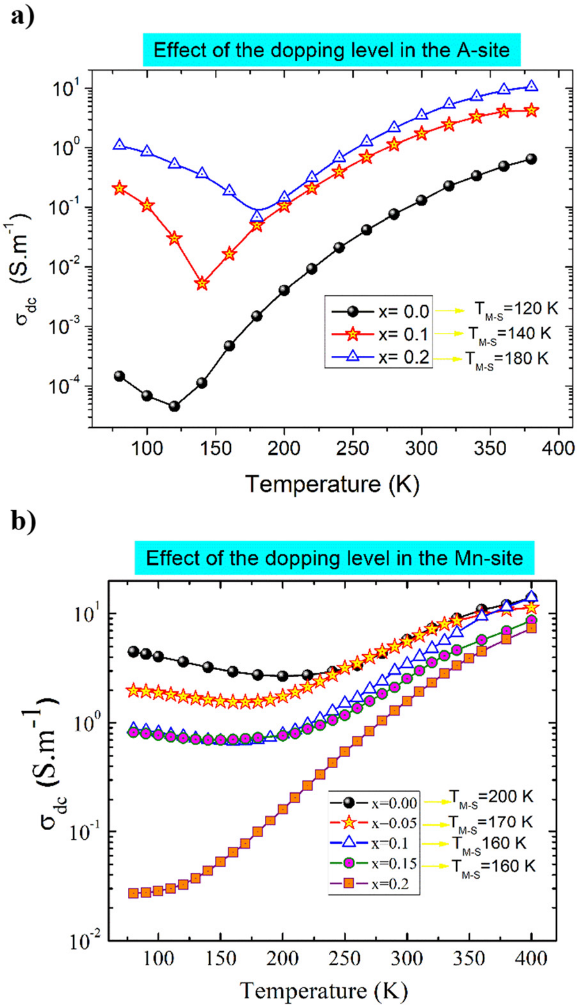

Fig. 8 Temperature dependence of the electrical dc-conductivity for $Sm_{0.55-x}Pr_xSr_{0.45}MnO_3$ (x = 0.0, 0.1, and 0.2) (a) ref. 36 and $La_{0.6}Sm_{0.1}Ba_{0.33}Mn_{1-x}Al_xO_3$ (x = 0.0, 0.05, 0.1, 0.15, and, 0.2) systems (b). Panel (a) adapted from ref. 36 with permission from Elsevier, copyright 2025.

orders of magnitude when the concentration increases from x = 0.0 to x = 0.2. A comparative analysis of the investigated manganite systems indicates that the effect of the dopant concentration strongly depends on the substitution site. In general, A-site substitutions mainly tune the structural bandwidth through ionic-radius mismatch and lattice distortion effects, whereas B-site substitutions directly perturb the Mn^{3+}–O–Mn^{4+} conduction network and therefore produce stronger variations in activation energy, conductivity, and carrier localization. Moreover, moderate substitution levels may optimize the transport properties by balancing carrier hopping and structural distortion, while excessive substitution tends to suppress double-exchange interactions and increase electrical resistivity.

III.D Impact of the annealing temperature

Based on previously reported investigations,[37–39] it has been found that variation in the annealing temperature affects the ceramics morphology and the crystallographic lattice parameters of manganites. Accordingly, the increase in the sintering temperature implies particle densification, which, in turn, favors grain agglomeration. Fig. 9(a) illustrates the evolution of the electrical conductivity as a function of the temperature for the $La_{0.9}Sr_{0.1}MnO_3$ powders at three mean annealing temperatures (600 °C, 800 °C, and 1200 °C). At annealing temperatures of T_S = 600 °C and 800 °C, the reported results indicate that the studied $La_{0.9}Sr_{0.1}MnO_3$ manganite exhibits a transition from metallic to semiconducting behavior at a defined temperature T_{M-S}. The annealing temperature increase has mainly modified the electrical characteristics of the studied material, especially at low measured temperatures. Accordingly, we found that the sample annealed at 1200 °C exhibits a semiconducting behavior over the explored temperature domain. The conduction mechanism, at low temperatures, was analyzed using the variable range hopping (VRH) model by fitting the experimental transport data, and the obtained agreement confirms the validity of this model for the highly annealed sample. In this case, the high annealing temperature value favors the presence of the variable range hopping conduction process. This behavior may be associated with enhanced carrier localization induced by annealing-dependent microstructural and structural modifications. For $La_{0.9}Sr_{0.1}MnO_3$, the TEM analysis (see Fig. 5) indicates that the increase in the annealing temperature induces a continuous microstructural transition from a nanostructured, highly agglomerated state to a well-sintered microcrystalline structure with significantly enlarged and more faceted grains. This evolution reflects progressive grain growth, densification, and a substantial reduction in grain-boundary density and structural disorder. Such microstructural refinement directly influences the transport behavior by modifying the relative contributions of grain interiors and grain boundaries to charge conduction. At low annealing temperatures, the high density of disordered grain boundaries is expected to dominate transport through strong scattering and barrier effects. In contrast, higher annealing temperatures promote improved crystallinity within grains and more compact intergranular connectivity, thereby reducing boundary-related disorder and reshaping carrier transport pathways. At elevated temperatures, all annealed samples exhibit an increase in electrical conductivity with temperature, which can be attributed to thermally activated charge carriers

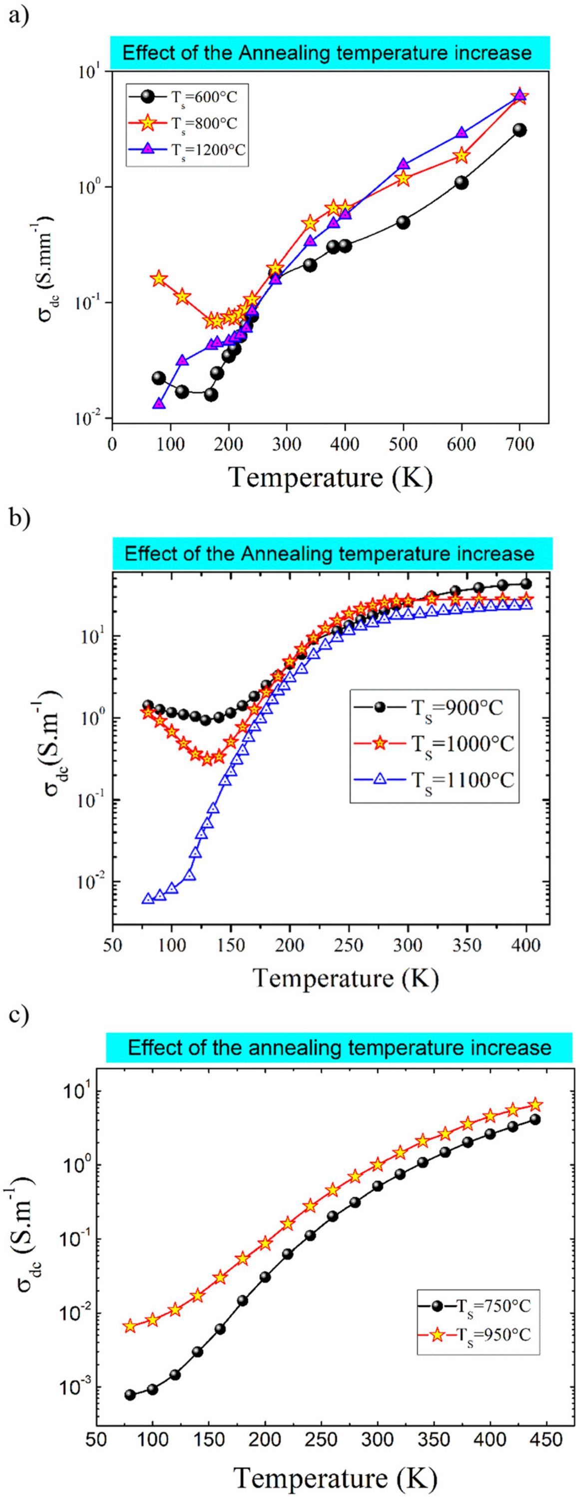

Fig. 9 Temperature dependence of the electrical dc-conductivity for two different annealed manganites: $La_{0.9}Sr_{0.1}MnO_3$ with T_S = 600 °C, T_S = 800 °C and T_S = 1200 °C (a); $La_{0.4}Bi_{0.3}Sr_{0.2}Ba_{0.1}MnO_3$ (T_S = 900 °C, 1000 °C and 1100 °C) (b); and $La_{0.5}Eu_{0.2}Ba_{0.3}MnO_3$ with T_S = 750 °C and T_S = 950 °C (c).

participating in SPH transport. In this regime, thermal energy enhances carrier mobility by facilitating hopping between localized states, leading to an overall increase in conductivity. This behavior is commonly observed in oxide-based manganite systems, where strong electron–phonon interactions favor polaron formation and thermally assisted hopping conduction. A similar temperature-dependent conductivity trend has also been reported in related perovskite manganites such as the $La_{0.4}Bi_{0.3}Sr_{0.2}$-$Ba_{0.1}MnO_3$

(T_S = 900 °C, 1000 °C, and 1100 °C) system (see Fig. 9(b), confirming that SPH-type conduction is a robust mechanism governing high-temperature transport in these materials. In this case, the increase in annealing temperature suppresses the metal-semiconductor transition and extends the semiconducting behavior over the entire measured temperature range. The effect of the sintering temperature increase is particularly pronounced in the low-temperature region, where the electrical conductivity is reduced by more than two orders of magnitude due to the enhanced localization of charge carriers and the strengthening of disorder-induced scattering effects. In this regime, the transport mechanism is better described by VRH, where carriers move between localized states in a thermally assisted tunneling process. This indicates that increased annealing temperature promotes structural reorganization that favors carrier localization rather than long-range metallic transport. For the $La_{0.5}Eu_{0.2}$-$Ba_{0.3}MnO_3$ system with T_S = 750 °C and T_S = 950 °C, it is observed from Fig. 9(c) that the variation in annealing temperature does not significantly alter the overall semiconducting nature of the material, suggesting that the conduction mechanism remains dominated by hopping transport across localized states regardless of sintering conditions.

However, it does not alter the fundamental relationship between the electrical conductivity and the underlying crystal chemistry, which is governed by Mn–O bond length and Mn–O–Mn bond angle distortions. Accordingly, for the $La_{0.5}Eu_{0.2}$-$Ba_{0.3}MnO_3$ system, the increase in annealing temperature from T_S = 750 °C to T_S = 950 °C is accompanied by an increase in the average Mn–O bond length from 1.950 Å to 1.973 Å, indicating a subtle modification of the local lattice distortion and the MnO_6 octahedral environment, which can influence the electron bandwidth and hopping probability. These structural parameters were determined from the Rietveld refinement of X-ray diffraction data reported in ref. 40. Additionally, such an effect favors the remarkable decrease of the $\langle$Mn–O–Mn$\rangle$ from $172.22(14)^\circ$ to $163.13\ (6)^\circ$, which modifies the overlap between Mn 3d and O 2p orbitals and consequently affects the charge carrier transport mechanism.[40] As a result, the transport properties are significantly influenced, leading to an enhancement of the electrical conductivity over the explored temperature range. The comparison between the investigated manganite systems indicates that the influence of annealing temperature cannot be generalized universally for all compositions. Although the increase in the annealing temperature often improves crystallinity, grain growth, and grain connectivity, excessive annealing may also favor carrier localization through oxygen non-stoichiometry, microstructural rearrangements, or enhanced structural distortion. Consequently, the optimization of the annealing conditions requires a compromise between improved crystallinity and preservation of favorable charge-transport pathways.

III.E Impact of the A-site cation deficiency

Recent investigations have shown that the introduction of A-site deficiency in manganite systems significantly modifies their physical properties.[41–43] For the $La_{0.65}Ba_{0.35-x}\square_xMnO_3$ ($0.0 \le x \le 0.2$), $La_{0.6}Sr_{0.2}Ba_{0.2-x}\square_xMnO_3$ ($0 \le x \le 0.15$), and $La_{0.5}Eu_{0.2}Ba_{0.2}\square_{0.1}MnO_3$ lacunar systems, it has been demonstrated that A-site vacancies serve as an effective tuning parameter for tailoring the structural, electronic, and transport properties. These vacancies play a key role in adjusting the Mn^{3+}/Mn^{4+} ratio, local lattice distortions, and carrier localization effects, thereby enabling controlled modification of the physicochemical behavior for targeted applications. Early investigations indicate that the increase in the vacancy concentration mainly modifies the average A-site ionic radius $\langle r_A \rangle$ in manganite systems.[41–43] This variation leads to significant changes in the lattice parameters and promotes deformation of the MnO_6 octahedra, which is reflected in the pronounced modification of both the Mn–O–Mn bond angles and Mn–O bond distances. In addition, the introduction of A-site vacancies alters the Mn^{3+}/Mn^{4+} ratio, with a particular reduction in the Mn^{4+} content due to charge compensation mechanisms. These structural and compositional modifications directly influence the electronic bandwidth and carrier hopping pathways, thereby strongly affecting the electrical properties and charge carrier dynamics in manganite oxides. Unlike oxygen vacancies, which mainly modify the oxygen stoichiometry and local electronic compensation, A-site cation vacancies directly alter the average ionic radius, the structural distortion of the MnO_6 octahedra, and the Mn^{3+}/Mn^{4+} ratio. Consequently, cation deficiency strongly affects the double-exchange interaction, carrier localization, and electrical transport behavior in manganite systems. In the present work, the impact of the deficiency concentration is examined for two kinds of manganite materials in the Ba and the Na sites. For the $La_{0.5}Eu_{0.2}$-$Ba_{0.3-x}\square_xMnO_3$ system, with x = 0.00, 0.05, and = 0.15,[44] the temperature dependence of the electrical conductivity is shown in Fig. 10(a). The obtained results indicate that the creation of Ba deficiency improves the electrical conductivity without affecting the material's semiconductor behavior. In this case, the increase of the Ba deficiency concentration mainly affects the material's structural properties. Accordingly, the increase of the Ba concentration leads to an increase in the Mn–O distance from d_{Mn-O} = 1.950 Å for x = 0.0 to 1.969 Å for x = 0.15. Moreover, the increase of the Ba deficiency decreases the average $\langle$Mn–O–Mn$\rangle$ angle from $172.22(14)^\circ$ for x = 0.0 to $163.93(8)^\circ$ for x = 0.15. However, for the $La_{0.8}Na_{0.2-x}\square_xMnO_3$ system, the reported results in Fig. 10(b) show that the increase of the sodium deficiency affects both the transition temperature value and electrical conductivity order. Accordingly, we found that the transition temperature has decreased from T_{M-S} = 220 K for $La_{0.8}Na_{0.2}MnO_3$ to reach T_{M-S} = 120 K for $La_{0.8}\square_{0.2}MnO_3$.

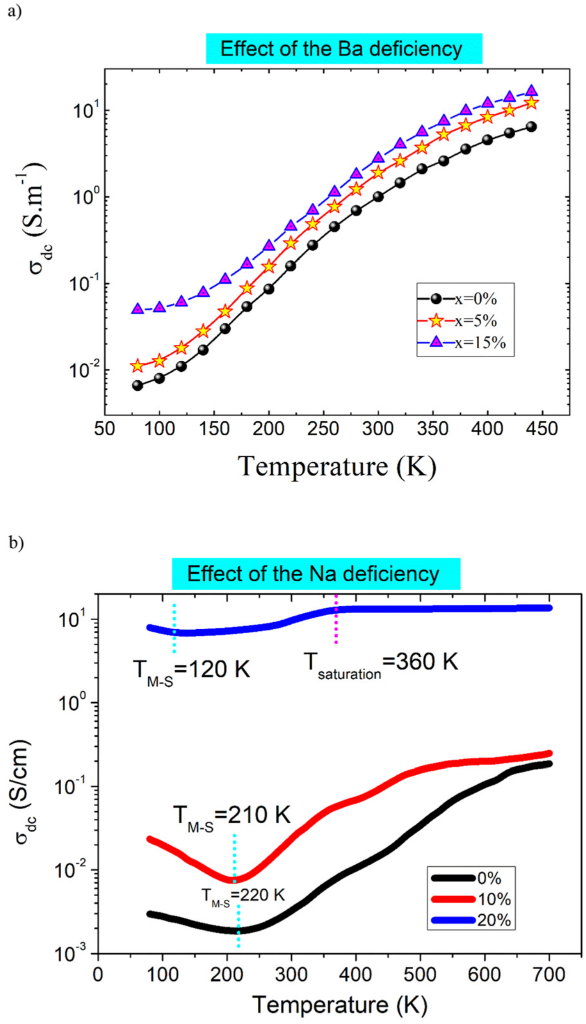

Fig. 10 Temperature dependence of the electrical dc-conductivity for two different lacunar manganites: $La_{0.5}Eu_{0.2}Ba_{0.3-x}\square_xMnO_3$ with x = 0.00, 0.05 and x = 0.15 (a) ref. 44; and $La_{0.8}Na_{0.2-x}\square_xMnO_3$ with x = 0.0, 0.1 and x = 0.2 (b) ref. 1. Panel (a) adapted from ref. 44 with permission from Elsevier, copyright 2025. Panel (b) adapted from ref. 1 with permission from Elsevier, copyright 2025.

This behavior can be explained by the fact that sodium deficiency modifies the charge compensation mechanism and consequently alters the Mn^{3+}/Mn^{4+} ratio. The resulting imbalance induces additional distortions in the MnO_6 octahedra, leading to an increase in the Mn–O bond length and a decrease in the Mn–O–Mn bond angle. Such structural changes weaken the double-exchange interaction between Mn^{3+} and Mn^{4+} ions by reducing the overlap between Mn 3d and O 2p orbitals, thereby suppressing electron hopping and enhancing charge carrier localization. Consequently, the metal–semiconductor transition temperature shifts toward lower values with increasing sodium deficiency.[45] In addition, the creation of the sodium deficiency (x = 0.2) favors the appearance of a conductivity saturation at T_{sat} = 360 K. Moreover, the plotted results indicate that the increase of sodium deficiency mainly increases the electrical conductivity order that rises by more than four orders of magnitude. Furthermore, the SEM micrographs of the $La_{0.8}Na_{0.2-x}\square_xMnO_3$ (x = 0.00, 0.05, 0.10, and 0.15) ceramics show that A-site sodium deficiency strongly affects the microstructure (see Fig. 6). The stoichiometric sample (x = 0.00) exhibits a heterogeneous polycrystalline morphology with agglomerated, faceted grains and a broad grain size distribution extending beyond 10 μm. With increasing Na deficiency, the microstructure progressively evolves toward more homogeneous, rounded, and less agglomerated grains, accompanied by a clear grain refinement from 5.55 μm (x = 0.00) to 3.26 μm (x = 0.15). This reduction in grain size is attributed to vacancy-induced suppression of grain growth during sintering, where A-site defects reduce diffusion kinetics and may promote grain-boundary pinning through solute-drag effects. Consequently, A-site deficiency acts as an effective parameter for controlling microstructural refinement. These changes are expected to influence the transport properties by increasing grain-boundary contributions to carrier scattering as the grain size decreases. Therefore, the electrical response is governed not only by changes in Mn^{3+}/Mn^{4+} chemistry and MnO_6 distortions but also by microstructural effects. In this work, grain-boundary contributions are qualitatively inferred from SEM and conductivity data, while a quantitative separation would require impedance spectroscopy.

III.F Temperature coefficient of resistance (TCR): analysis and applications

The temperature coefficient of resistance (TCR) is a key parameter used to evaluate the sensitivity of electrical transport to temperature variations. It is defined as[46,47]

$$\mathrm{TCR} = \frac{1}{R(T)}\frac{\mathrm{d}R(T)}{\mathrm{d}T} \times 100\ \left(\%\ \mathrm{K}^{-1}\right)$$

or equivalently in terms of resistivity

$$\mathrm{TCR} = \frac{1}{\rho(T)}\frac{\mathrm{d}\rho(T)}{\mathrm{d}T} \times 100\ \left(\%\ \mathrm{K}^{-1}\right)$$

Depending on the sign of dR/dT, two distinct behaviors are identified.[48–51] A negative temperature coefficient (NTCR) corresponds to semiconducting behavior ($dR/dT < 0$), typically governed by thermally activated conduction mechanisms. In contrast, a positive temperature coefficient (PTCR) ($dR/dT > 0$) is associated with metallic-like conduction and is often observed near the metal–insulator transition. Within the thermally activated regime, the resistance follows an Arrhenius-type relation:[48–51]

$$R(T) = R_0 \exp\left(\frac{E_a}{k_B \cdot T}\right)$$

which leads to

$$\mathrm{TCR} = -\frac{E_a}{k_B \cdot T^2} \times 100$$

This expression indicates that large activation energies result in high NTCR values, particularly at low temperatures. In addition to the TCR magnitude, the absolute resistance level at the operating temperature is also an important parameter for thermistor applications, as it directly affects power consumption, the signal-to-noise ratio, and compatibility with electronic readout circuits. In manganite systems, the resistance value strongly depends on the composition, microstructure, and processing conditions such as annealing temperature. Consequently, a wide range of resistance levels can be achieved, which is beneficial for tuning these materials for specific sensing applications. Fig. 11–17 show the variation of TCR as a function of temperature for all investigated manganite systems. In most cases, a pronounced peak is observed, corresponding to maximum sensitivity at a characteristic temperature. For certain compositions, a second peak appears at higher temperatures, indicating the coexistence of different conduction regimes. The extracted NTCR and PTCR values, along with their corresponding peak temperatures, are summarized in Table 1. A comparative analysis reveals that the TCR behavior is strongly influenced by several intrinsic and extrinsic parameters. In the $Pr_{0.65}Ca_{0.25}X_{0.1}MnO_3$ series (X = Ba, Cd, Sr, and Pb), the nature of the A-site dopant plays a crucial role. The Cd- and Pb-substituted samples exhibit significantly enhanced NTCR values (-20.05 and $-24.03\%\cdot K^{-1}$, respectively), whereas the Ba-doped compound shows the emergence of a secondary peak at higher temperature (240 K). These variations can be attributed to differences in ionic radii and the resulting lattice distortions, which affect the Mn–O–Mn bond angle and, consequently, the electron hopping probability. Indeed, substitution with A-site cations of different ionic radii modifies the tolerance factor and induces distortions of the MnO_6 octahedra. These structural distortions alter the Mn–O–Mn bond angle, thereby changing the overlap between Mn 3d and O 2p orbitals that governs the double-exchange interaction.[40] A decrease in the Mn–O–Mn bond angle reduces the electron transfer integral and suppresses carrier hopping, resulting in stronger charge localization and a sharper variation of resistivity with temperature. Consequently, the temperature coefficient of resistance (TCR) is significantly affected, leading to the enhanced NTCR behavior observed for the Cd- and Pb-substituted samples. In the $Pr_{0.7}Ca_{0.3}Mn_{0.9}X_{0.1}O_3$ system (X = Co, Ni, Fe, and Cr), B-site substitution directly modifies the double exchange interaction. Among these compounds, Cr doping leads to the highest NTCR value ($-35.05\%\cdot K^{-1}$), indicating strong carrier localization. This behavior arises from the disruption of Mn^{3+}–O–Mn^{4+} conduction pathways, which enhances the activation energy and reinforces the semiconducting character. The effect of the dopant concentration is illustrated in the $La_{0.6}Sm_{0.1}Ba_{0.33}Mn_{1-x}Al_xO_3$ series. Here, moderate NTCR values are observed, ranging from -1.36 to $-2.51\%\cdot K^{-1}$. For x = 0.05, the appearance of two TCR peaks suggests the coexistence of distinct conduction mechanisms. The substitution

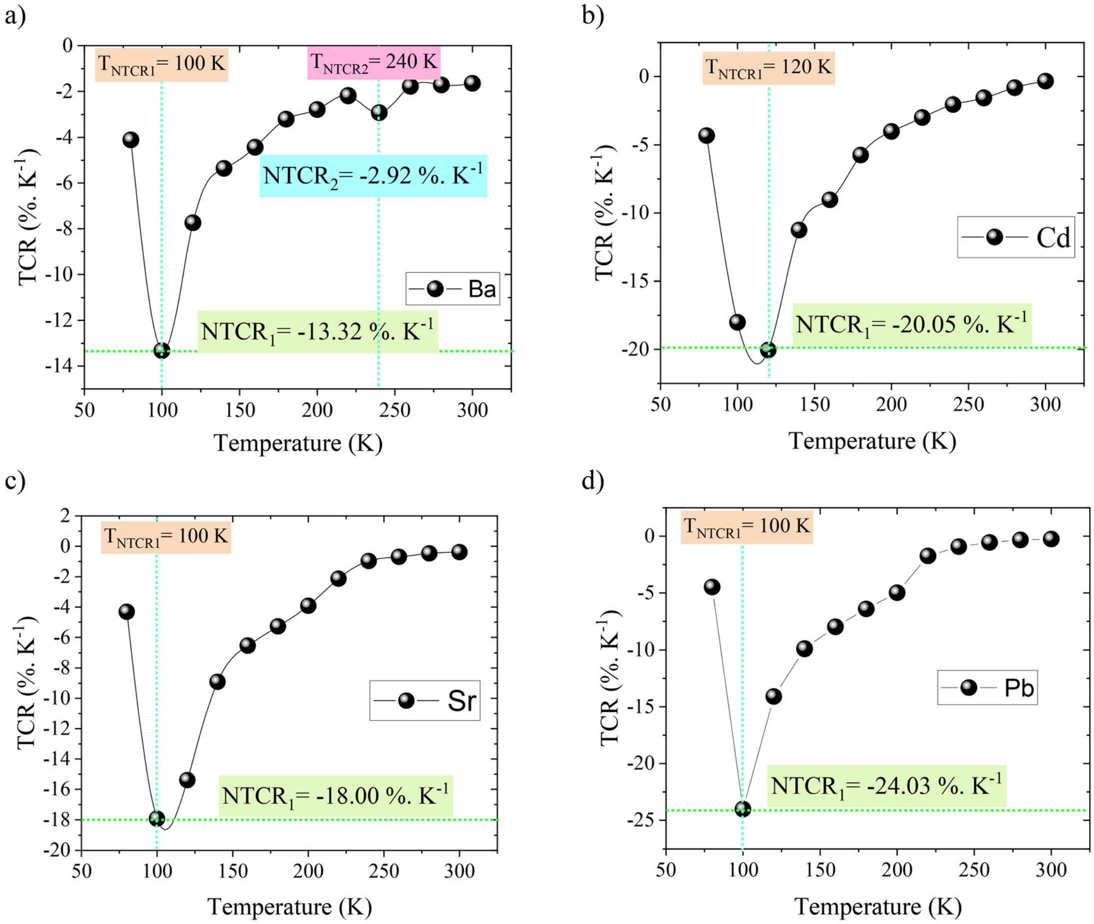

Fig. 11 Variation of the temperature coefficient of resistance (TCR) *versus* the impact of the nature of the doping element on the A site $Pr_{0.65}Ca_{0.25}X_{0.1}MnO_3$ (X = Ba, Cd, Sr and Pb).

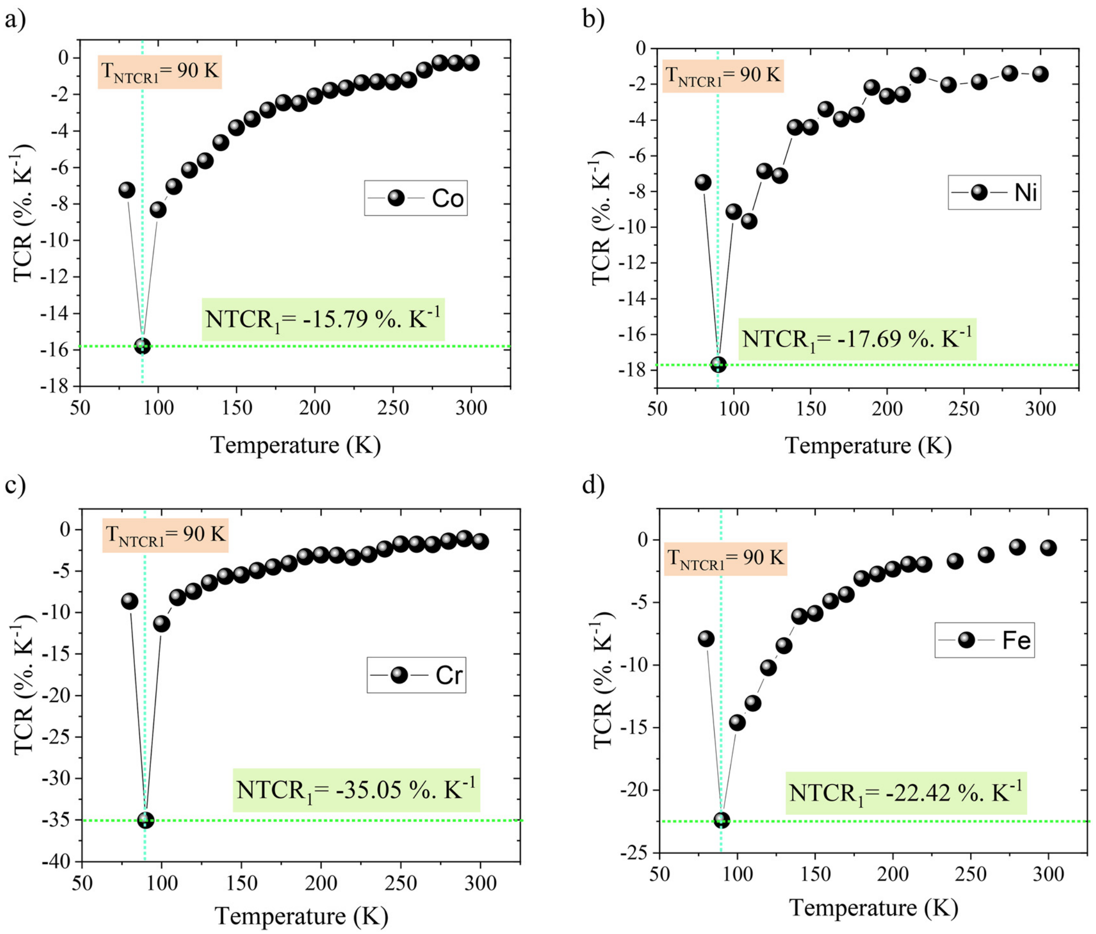

Fig. 12 Temperature dependence of the temperature coefficient of resistance (TCR) *vs.* the impact of the nature of the doping element on the B site $Pr_{0.7}Ca_{0.3}Mn_{0.9}X_{0.1}O_3$ (X = Co, Ni, Cr and Fe).

of Mn by non-magnetic Al^{3+} weakens the double exchange interaction, leading to reduced conductivity and broadened transition features. The annealing temperature also has a significant impact on TCR behavior. In $La_{0.9}Sr_{0.1}MnO_3$, an increase in the sintering temperature from 600 °C to 1200 °C results in a decrease in NTCR magnitude followed by the appearance of a secondary peak at higher temperature. Similarly, in $La_{0.4}Bi_{0.3}Sr_{0.2}Ba_{0.1}MnO_3$, the NTCR value increases markedly (from −3.32 to −12.97%·K^{-1}) with increasing annealing temperature. These trends are associated with improved crystallinity, enhanced grain connectivity, and reduced grain boundary resistance. In contrast, lacunar systems such as $La_{0.5}Eu_{0.2}Ba_{0.3-x}\square_xMnO_3$ and $La_{0.8}Na_{0.2-x}\square_xMnO_3$ exhibit PTCR behavior, with positive values reaching up to 3.24%·K^{-1}. The introduction of cation vacancies modifies the Mn^{3+}/Mn^{4+} ratio and carrier concentration, which can induce metallic-like conduction and lead to a positive TCR response. A comparison with previously reported manganites shows that the obtained TCR values are competitive. For example, $Sm_{0.55}Sr_{0.45}MnO_3$ exhibits an NTCR of −9.60%·K^{-1}, while $Pr_{0.7}Ca_{0.3}Mn_{0.98}Cr_{0.02}O_3$ shows dual peaks with values of −13.92 and −7.13%·K^{-1}. Notably, the Cr-doped compositions investigated in this work display superior TCR performance, highlighting the effectiveness of compositional tuning. The observed TCR behavior can be understood in terms of the interplay between several conduction mechanisms.[52] The double exchange interaction governs metallic conduction and is responsible for PTCR behavior, whereas small polaron hopping dominates in the insulating regime, leading to NTCR characteristics. Additionally, grain boundary effects contribute to the overall resistance, particularly at low temperatures, and may give rise to secondary TCR peaks. The comparative TCR analysis demonstrates that the highest NTCR responses are generally obtained in systems combining strong carrier localization with moderate electrical conductivity. In contrast, systems exhibiting enhanced metallic conduction tend to show reduced NTCR magnitudes but may develop PTCR characteristics near the metal–semiconductor transition. These observations highlight that optimizing thermistor performance requires a careful balance between activation energy enhancement, carrier mobility, and conduction-path continuity. From an application perspective, manganites exhibiting high NTCR values near room temperature are promising candidates for infrared bolometers and thermal sensors. Although the present study provides a detailed analysis of intrinsic thermistor parameters such as TCR, activation energy (E_a), thermistor constant (β), and sensitivity parameter (α),

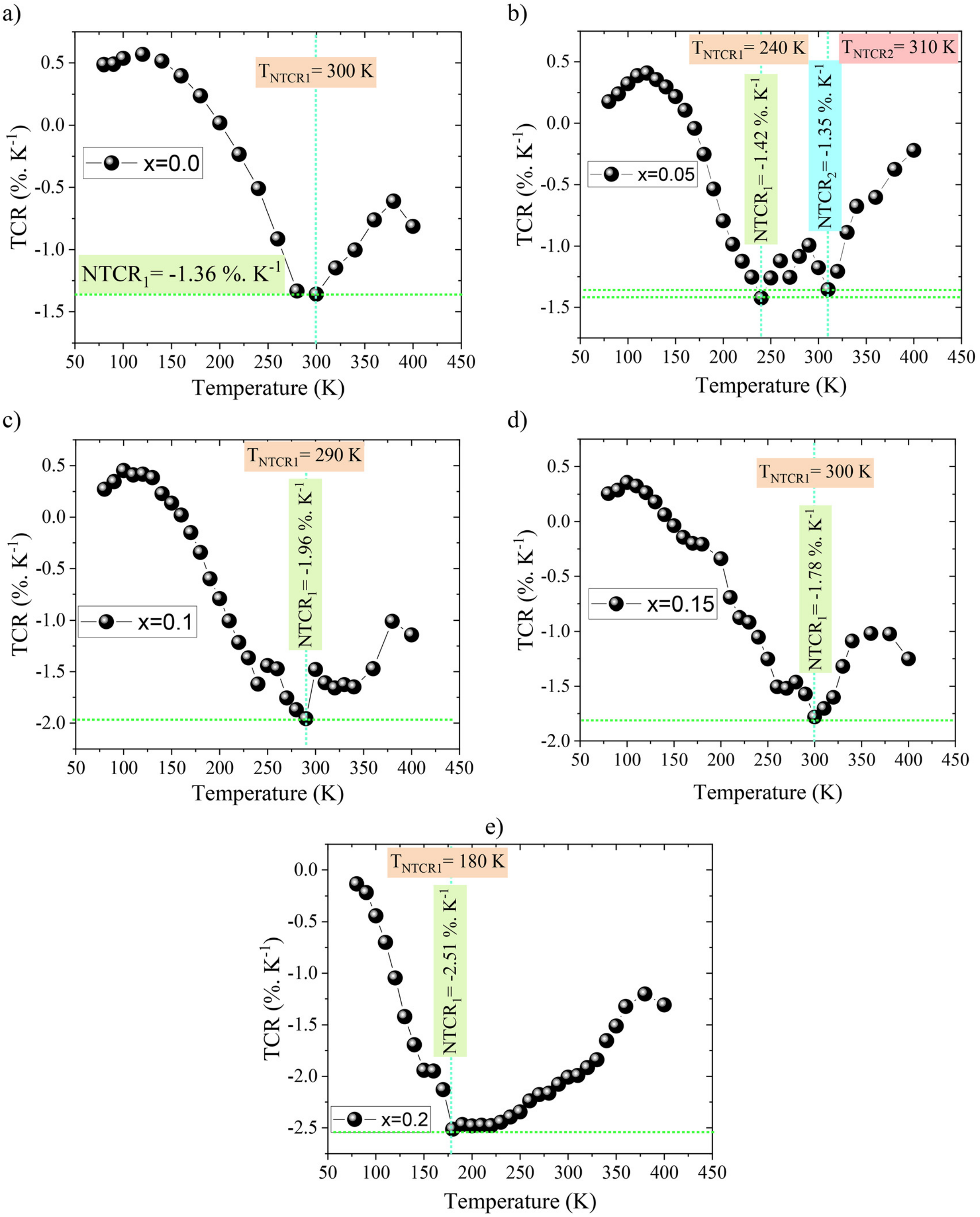

Fig. 13 Temperature dependence of the temperature coefficient of resistance (TCR) for the $La_{0.6}Sm_{0.1}Ba_{0.33}Mn_{1-x}Al_xO_3$ (x = 0.0, 0.05, 0.1, 0.15, and 0.2) system.

practical thermistor performance also depends on additional device-level characteristics. These include long-term stability, thermal hysteresis, reproducibility, response time, ageing effects, and thermal cycling durability. These parameters are essential for real device applications and sensor reliability. However, their evaluation requires dedicated device fabrication and systematic time-dependent and cycling experiments, which are beyond the scope of the present work. Nevertheless, the studied manganite systems exhibit promising intrinsic thermistor behavior, indicating their potential for further optimization toward practical sensor applications. Materials with PTCR behavior are suitable for self-regulating devices, such as circuit protection elements and heating components. Furthermore, the strong coupling between electrical transport and magnetic ordering in these systems makes them attractive for spintronic and multifunctional electronic applications. The TCR properties of manganites are highly tunable through careful control of dopant nature, concentration, annealing temperature,

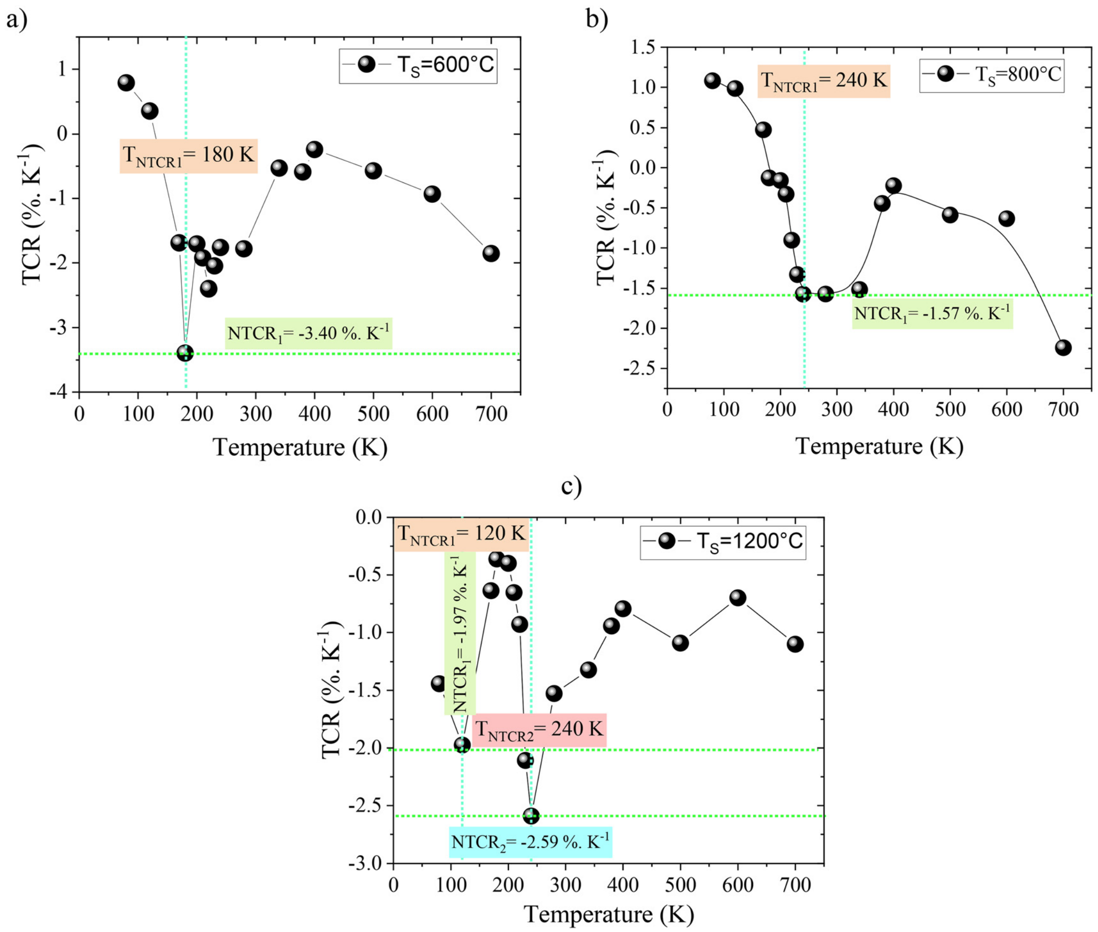

Fig. 14 Temperature dependence of the temperature coefficient of resistance (TCR) for $La_{0.9}Sr_{0.1}MnO_3$ with T_S = 600 °C, T_S = 800 °C and T_S = 1200 °C.

and cation deficiency. The wide range of achievable TCR values, including very high NTCR values (up to $-35\%\cdot K^{-1}$) and significant PTCR responses, underscores the potential of these materials for advanced thermal sensing and electronic device applications. In comparison with conventional commercial thermistors, particularly NTC devices based on transition metal oxide spinels (such as Mn–Ni–Co systems), the manganite materials investigated in this work exhibit competitive TCR and activation energy values.[53–56] Moreover, their strong tunability through doping, cation deficiency, and thermal processing offers an additional advantage over conventional materials. This tunability makes manganites promising candidates for next-generation oxide-based thermistors, especially for multifunctional and application-specific sensing devices.

III.G Activation energy, thermistor constant (*β*), and sensitivity parameter (*α*)

The electrical transport behavior of manganite systems can be further quantified through activation energy (E_a), thermistor constant (β), and temperature sensitivity parameter (α). These parameters provide complementary insight into the conduction mechanism and are particularly relevant for thermistor applications. In this work, E_a is extracted from the slope of the linear fit of $\ln(\rho)$ or $\ln(R)$ *versus* $1/T$, with high correlation coefficients ($R^2 \approx 0.98$–0.99) confirming the validity of the thermally activated conduction model for all investigated systems. The thermistor constant β, widely used in NTC thermistors, is defined as[48–51]

$$\beta = \frac{E_a}{k_B}$$

This parameter reflects the thermal activation strength of the conduction process. Temperature sensitivity parameter α is expressed as[57,58]

$$\alpha = -\frac{\beta}{T^2} \times 100$$

This relation indicates that α is directly governed by β and inversely proportional to the square of temperature. The negative sign confirms the NTCR behavior observed in most of the studied compounds. The extracted values of E_a, β, and α for all investigated manganites are summarized in Table 2. A detailed comparative analysis reveals that these parameters are highly sensitive to the composition, dopant nature, concentration, and processing conditions. In the $Pr_{0.65}Ca_{0.25}X_{0.1}MnO_3$ series (X = Ba, Cd, Sr, and Pb), the activation energy ranges from 95 to 116 meV, with corresponding β values between 1102 and 1346 K. The highest values are obtained for Cd substitution

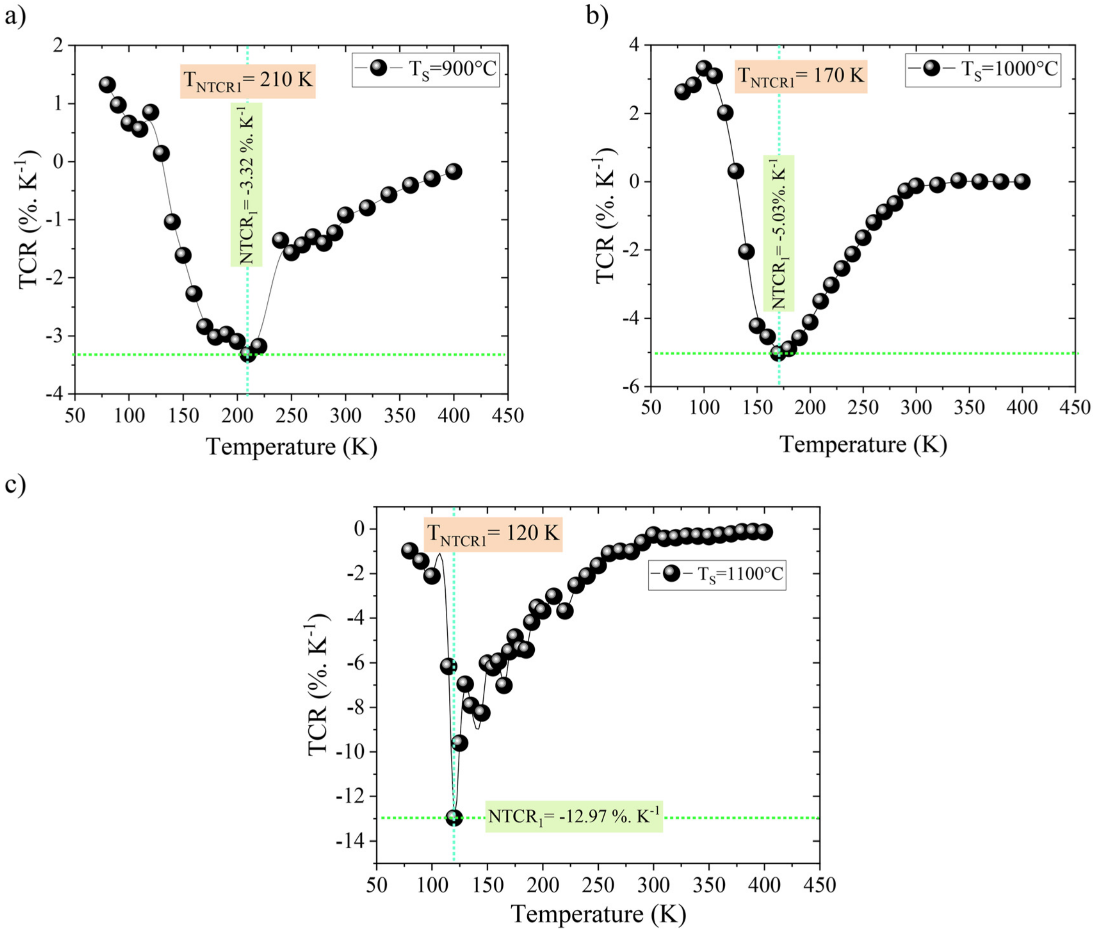

Fig. 15 Temperature dependence of the temperature coefficient of resistance (TCR) for $La_{0.4}Bi_{0.3}Sr_{0.2}Ba_{0.1}MnO_3$ (T_S = 900 °C, 1000 °C and 1100 °C).

(116 meV, 1346 K), which correlates with the highest magnitude of α ($-1.50\%\cdot K^{-1}$). This behavior reflects enhanced carrier localization induced by lattice distortion and reduced bandwidth, consistent with the strong NTCR response discussed previously. For the $Pr_{0.7}Ca_{0.3}Mn_{0.9}X_{0.1}O_3$ series (X = Co, Ni, Cr, and Fe), the activation energy spans from 70 to 98 meV. The Co-doped sample exhibits the lowest values (70 meV, 812 K, $-0.90\%\cdot K^{-1}$), indicating relatively easier carrier hopping, while Cr doping significantly increases these parameters (98 meV, 1137 K, $-1.26\%\cdot K^{-1}$). This trend highlights the strong influence of B-site substitution on the double exchange mechanism and the associated energy barriers for conduction. A more pronounced variation is observed in the $La_{0.6}Sm_{0.1}Ba_{0.33}Mn_{1-x}Al_xO_3$ series. With increasing Al content, the activation energy increases markedly from 93 meV (x = 0) to 155 meV (x = 0.20), accompanied by a corresponding increase in β (from 1079 to 1799 K) and α (from -1.2 to $-2.0\%\cdot K^{-1}$). This behavior is attributed to the substitution of Mn by non-magnetic Al^{3+} ions, which weakens the double exchange interaction and enhances carrier localization, thereby increasing the energy barrier for hopping conduction. The influence of annealing temperature is clearly observed in the $La_{0.9}Sr_{0.1}MnO_3$ system. An increase in the sintering temperature from 600 °C to 1200 °C leads to a significant increase in activation energy (78 to 133 meV), β (905 to 1543 K), and α (-1.01 to $-1.71\%\cdot K^{-1}$). A similar trend is observed in $La_{0.4}Bi_{0.3}Sr_{0.2}Ba_{0.1}MnO_3$, where the E_a increases from 108 to 130 meV with increasing annealing temperature. These results indicate that improved crystallinity and reduced grain boundary scattering enhance the intrinsic transport mechanism, leading to higher activation energies. In lacunar systems such as $La_{0.5}Eu_{0.2}Ba_{0.3-x}\square_xMnO_3$, the activation energy remains relatively high ($\sim$143–145 meV), with β values around 1659–1683 K and α values close to $-1.85\%\cdot K^{-1}$. The presence of cation vacancies modifies the Mn^{3+}/Mn^{4+} ratio and introduces additional disorder, which stabilizes a thermally activated conduction regime despite the PTCR behavior observed in certain temperature ranges. The highest activation energies in this study are obtained for the $La_{0.8}Na_{0.2-x}\square_xMnO_3$ system, reaching up to 290 meV, with a corresponding β value of 3366 K and an α value of $-3.74\%\cdot K^{-1}$. These large values indicate strong carrier localization and high thermal sensitivity, making these compounds particularly suitable for high-performance thermistor applications. In contrast, the lowest values are observed for $La_{0.8}\square_{0.2}MnO_3$ (47 meV, 545 K, $-0.60\%\cdot K^{-1}$), reflecting a reduced activation barrier and weaker temperature dependence. A comparison with related manganite

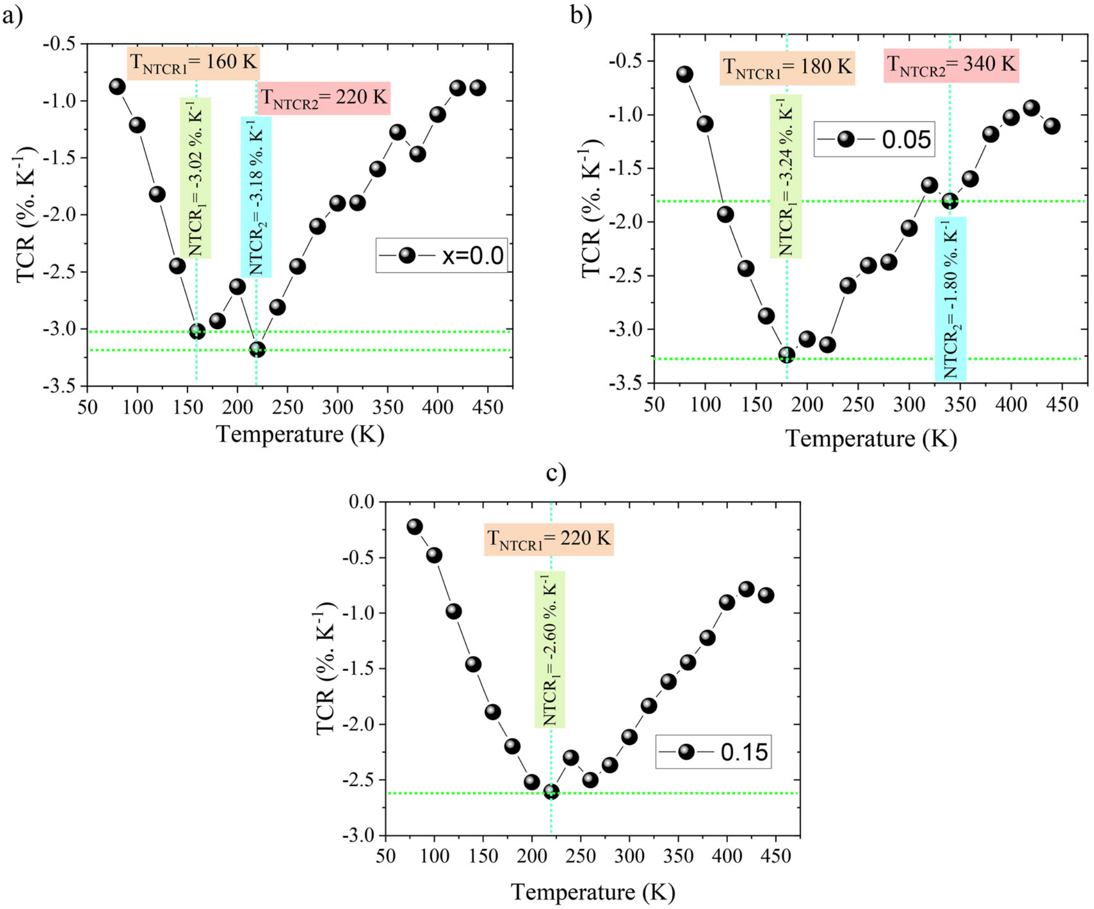

Fig. 16 Temperature dependence of the temperature coefficient of resistance (TCR) for $La_{0.5}Eu_{0.2}Ba_{0.3-x}\square_xMnO_3$ with x = 0.00, 0.05 and 0.15.

systems from the literature, such as $Sm_{0.55}Sr_{0.45}MnO_3$ (200 meV, 2321 K, $-2.58\%\cdot K^{-1}$) and $Sm_{0.45}Pr_{0.1}Sr_{0.45}MnO_3$ (168 meV, 1949 K, $-2.17\%\cdot K^{-1}$), confirms that the present results cover a wide range of activation energies and sensitivities. Notably, the Na-deficient and Al-rich compositions exhibit comparable or superior performance in terms of β and α, demonstrating the effectiveness of compositional engineering. A global comparison between the investigated systems reveals that the activation energy, thermistor constant β, and sensitivity parameter α are strongly correlated with the degree of structural disorder and carrier localization. Systems exhibiting strong lattice distortion and suppressed double-exchange interactions generally display larger activation energies and higher thermistor sensitivity. These results confirm that high-performance manganite thermistors require an optimized compromise between activation-energy enhancement and preservation of sufficient carrier mobility. Generally, a strong correlation is observed between E_a, β, and α, as expected from their theoretical relationships. Materials with higher activation energies systematically exhibit larger β values and higher sensitivity (α), confirming that these parameters are intrinsically linked. This correlation also aligns with the TCR analysis, where higher E_a values correspond to stronger NTCR behavior. From an application standpoint, materials with high β (typically > 2000 K) and large α are highly desirable for thermistor and infrared sensing applications. In this context, the $La_{0.8}Na$-based and Sm-based manganites emerge as promising candidates. Conversely, compositions with moderate E_a and β values offer stable and tunable responses suitable for multifunctional electronic devices. In summary, the systematic variation of activation energy, thermistor constant, and sensitivity parameter demonstrates that manganites provide a highly versatile platform for tailoring electrical transport properties. The strong dependence of these parameters on structural and compositional factors highlights the crucial role of dopant engineering and processing conditions in optimizing performance for specific technological applications.[57,58]

III.H Comparative synthesis, unresolved issues, and design principles for high-performance manganite thermistors

The preceding sections present the influence of multiple compositional and processing parameters on the electrical transport behavior of manganite systems. To synthesize these results and provide a critical comparison between the investigated compounds, the main correlations between structural parameters, transport mechanisms, and thermistor performance are summarized in Fig. 18. Explicitly, Fig. 18 presents a schematic representation illustrating the relationships between

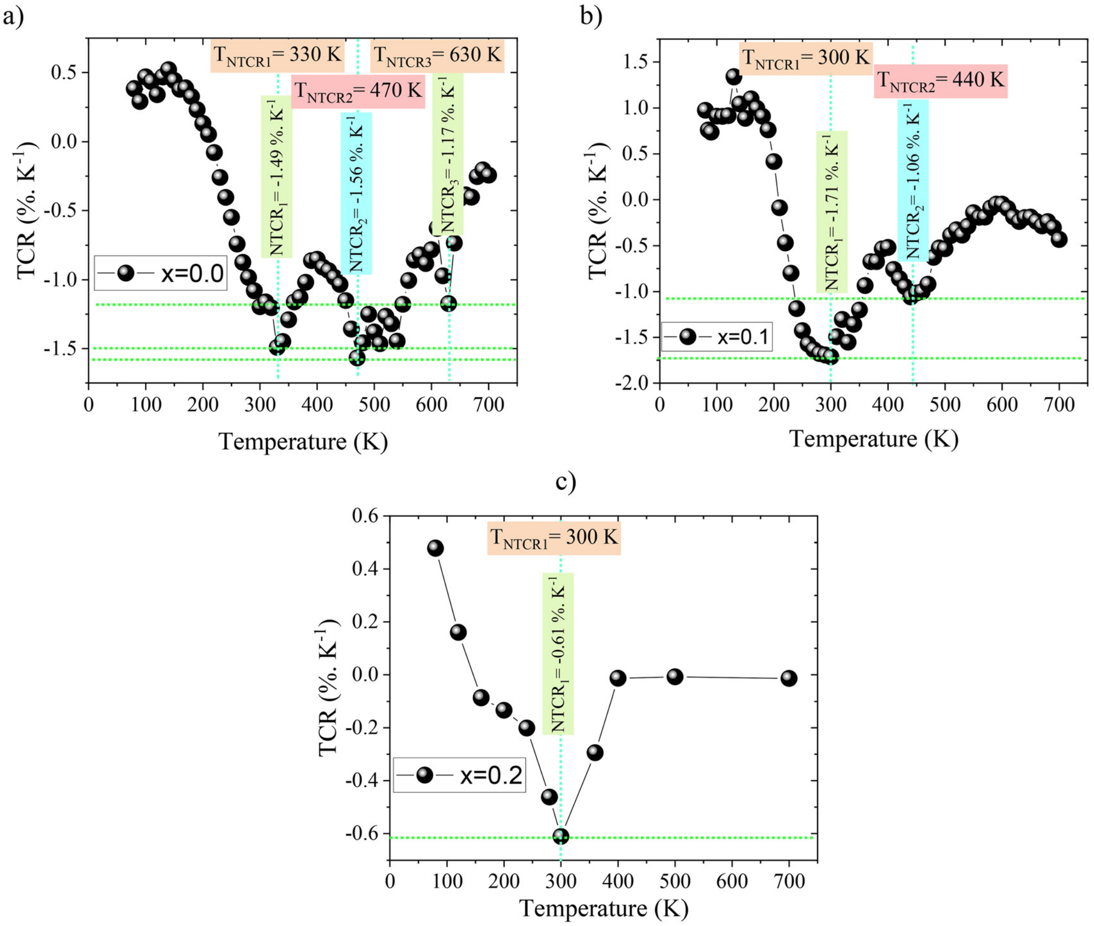

Fig. 17 Temperature dependence of the temperature coefficient of resistance (TCR) for $La_{0.8}Na_{0.2-x}\square_xMnO_3$ with x = 0.0, 0.1 and 0.2.

control parameters (dopant nature, dopant concentration, annealing temperature, and cation deficiency), the resulting structural modifications, the dominant transport mechanisms, and the corresponding thermistor performance. As illustrated in Fig. 18, the electrical transport properties of manganites are governed by a strong interplay between structural distortion, the carrier concentration, grain-boundary effects, and charge-carrier localization. Although the investigated systems differ in composition and preparation conditions, several common trends can be identified. First, the nature of the dopant element strongly controls the magnitude of lattice distortion through ionic-radius mismatch effects. As shown schematically in Fig. 18, substitutions at both A and B sites modify the Mn–O bond length and the Mn–O–Mn bond angle, thereby affecting the overlap between Mn 3d and O 2p orbitals and consequently the strength of the double-exchange interaction.[40,45] Dopants producing strong structural disorder generally favor charge localization, variable range hopping conduction, and enhanced NTCR behavior. In contrast, dopants promoting larger electronic bandwidths tend to improve carrier delocalization and electrical conductivity. Second, the dopant concentration plays a critical role in defining the balance between carrier localization and delocalization. Moderate substitution levels may optimize the Mn^{3+}/Mn^{4+} ratio and enhance carrier hopping through the stabilization of the double-exchange mechanism. However, excessive substitution can disrupt the Mn^{3+}–O–Mn^{4+} conduction pathways, increase activation energy, and suppress metallic conduction. The comparative analysis presented in Fig. 18 indicates that A-site substitutions mainly tune the structural bandwidth through ionic-radius effects, whereas B-site substitutions directly perturb the Mn conduction network and therefore produce stronger changes in activation energy and electrical conductivity. Third, the annealing temperature strongly influences the microstructure and grain connectivity of manganite ceramics. As summarized in Fig. 18, the increase in the annealing temperature generally improves crystallinity and grain growth, thereby reducing grain-boundary scattering and enhancing charge transport. Nevertheless, excessive annealing may also induce oxygen non-stoichiometry, structural rearrangements, or enhanced carrier localization, favoring variable range hopping conduction at low temperatures. Consequently, the optimization of the annealing conditions requires a compromise between improved crystallinity and preservation of favorable transport pathways. Fourth, cation deficiency emerges as an effective strategy for tuning both NTCR and PTCR behaviors. The schematic representation in Fig. 18 shows that vacancy creation modifies the Mn^{3+}/Mn^{4+} ratio, induces additional lattice distortions, and changes the carrier density. Depending on the

Table 1 The TCR values and the corresponding temperature for the studied manganites

Material	NTCR$_1$/PTCR (% K^{-1})	T_{NTCR_1}/T_{NTCR_1} (K)	NTCR$_2$ (% K^{-1})	T_{NTCR_2} (K)	Ref.
$Pr_{0.65}Ca_{0.25}Ba_{0.10}MnO_3$	−13.32	100	−2.92	240	This work
$Pr_{0.65}Ca_{0.25}Cd_{0.10}MnO_3$	−20.05	120	—	—	This work
$Pr_{0.65}Ca_{0.25}Sr_{0.10}MnO_3$	−18.00	100	—	—	This work
$Pr_{0.65}Ca_{0.25}Pb_{0.10}MnO_3$	−24.03	100	—	—	This work
$Pr_{0.7}Ca_{0.3}Mn_{0.90}Co_{0.10}O_3$	−15.79	90	—	—	This work
$Pr_{0.7}Ca_{0.3}Mn_{0.90}Ni_{0.10}O_3$	−17.69	90	—	—	This work
$Pr_{0.7}Ca_{0.3}Mn_{0.90}Cr_{0.10}O_3$	−35.05	90	—	—	This work
$Pr_{0.7}Ca_{0.3}Mn_{0.90}Fe_{0.10}O_3$	−22.42	90	—	—	This work
$La_{0.6}Sm_{0.1}Ba_{0.33}MnO_3$	−1.36	300	—	—	This work
$La_{0.6}Sm_{0.1}Ba_{0.33}Mn_{0.95}Al_{0.05}O_3$	−1.42	240	−1.35	310	This work
$La_{0.6}Sm_{0.1}Ba_{0.33}Mn_{0.90}Al_{0.10}O_3$	−1.96	290	—	—	This work
$La_{0.6}Sm_{0.1}Ba_{0.33}Mn_{0.85}Al_{0.15}O_3$	−1.78	300	—	—	This work
$La_{0.6}Sm_{0.1}Ba_{0.33}Mn_{0.80}Al_{0.20}O_3$	−2.51	180	—	—	This work
$La_{0.9}Sr_{0.1}MnO_3$ (T_S = 600 °C)	−3.40	180	—	—	This work
$La_{0.9}Sr_{0.1}MnO_3$ (T_S = 800 °C)	−1.57	240	—	—	This work
$La_{0.9}Sr_{0.1}MnO_3$ (T_S = 1200 °C)	−1.97	120	−2.59	240	This work
$La_{0.4}Bi_{0.3}Sr_{0.2}Ba_{0.1}MnO_3$ (T_S = 900 °C)	−3.32	210	—	—	This work
$La_{0.4}Bi_{0.3}Sr_{0.2}Ba_{0.1}MnO_3$ (T_S = 1000 °C)	−5.03	170	—	—	This work
$La_{0.4}Bi_{0.3}Sr_{0.2}Ba_{0.1}MnO_3$ (T_S = 1100 °C)	−12.97	120	—	—	This work
$La_{0.5}Eu_{0.2}Ba_{0.3}MnO_3$	3.02	160	3.18	220	This work
$La_{0.5}Eu_{0.2}Ba_{0.25}\square_{0.05}MnO_3$	3.24	180	1.80	340	This work
$La_{0.5}Eu_{0.2}Ba_{0.15}\square_{0.15}MnO_3$	2.60	220	—	—	This work
$La_{0.8}Na_{0.2}MnO_3$	1.49	330	1.56	470	This work
$La_{0.8}Na_{0.1}\square_{10}MnO_3$	1.71	300	1.06	440	This work
$La_{0.8}\square_{0.20}MnO_3$	0.61	300	—	—	This work
$Sm_{0.55}Sr_{0.45}MnO_3$	−9.60	160	—	—	36
$Sm_{0.45}Pr_{0.1}Sr_{0.45}MnO_3$	13.56	120	−7.00	160	36
$Sm_{0.35}Pr_{0.2}Sr_{0.45}MnO_3$	5.50	160	−4.25	220	36

type of vacancy and the host composition, this can either enhance carrier localization or stabilize metallic-like transport. Therefore, controlled deficiency engineering offers a flexible route for tailoring transition temperatures and thermistor sensitivity. The transport mechanisms summarized in Fig. 18 also reveal that the electrical behavior of manganites results from the competition between several conduction processes, including double exchange (DE),[40] small polaron hopping

Table 2 The deduced activation energy, thermistor constant (*β*), and sensitivity parameter (α) of the studied manganites

Material	E_a (meV)	R^2	*β* (K)	α (% K)	This work
$Pr_{0.65}Ca_{0.25}Ba_{0.10}MnO_3$	95	0.99	1102	−1.20	This work
$Pr_{0.65}Ca_{0.25}Cd_{0.10}MnO_3$	116	0.99	1346	−1.50	This work
$Pr_{0.65}Ca_{0.25}Sr_{0.10}MnO_3$	103	0.99	1195	−1.30	This work
$Pr_{0.65}Ca_{0.25}Pb_{0.10}MnO_3$	112	0.99	1299	−1.40	This work
$Pr_{0.7}Ca_{0.3}Mn_{0.90}Co_{0.10}O_3$	70	0.99	812	−0.90	This work
$Pr_{0.7}Ca_{0.3}Mn_{0.90}Ni_{0.10}O_3$	81	0.99	940	−1.04	This work
$Pr_{0.7}Ca_{0.3}Mn_{0.90}Cr_{0.10}O_3$	98	0.99	1137	−1.26	This work
$Pr_{0.7}Ca_{0.3}Mn_{0.90}Fe_{0.10}O_3$	96	0.99	1114	−1.24	This work
$La_{0.6}Sm_{0.1}Ba_{0.33}MnO_3$	93	0.99	1079	−1.2	This work
$La_{0.6}Sm_{0.1}Ba_{0.33}Mn_{0.95}Al_{0.05}O_3$	80	0.99	928	−1.1	This work
$La_{0.6}Sm_{0.1}Ba_{0.33}Mn_{0.90}Al_{0.10}O_3$	138	0.99	1601	−1.8	This work
$La_{0.6}Sm_{0.1}Ba_{0.33}Mn_{0.85}Al_{0.15}O_3$	120	0.99	1392	−1.5	This work
$La_{0.6}Sm_{0.1}Ba_{0.33}Mn_{0.80}Al_{0.20}O_3$	155	0.99	1799	−2.0	This work
$La_{0.9}Sr_{0.1}MnO_3$ (T_S = 600 °C)	78	0.90	905	−1.01	This work
$La_{0.9}Sr_{0.1}MnO_3$ (T_S = 800 °C)	98	0.90	1137	−1.26	This work
$La_{0.9}Sr_{0.1}MnO_3$ (T_S = 1200 °C)	133	0.90	1543	−1.71	This work
$La_{0.4}Bi_{0.3}Sr_{0.2}Ba_{0.1}MnO_3$ (T_S = 900 °C)	108	0.98	1253	−1.39	This work
$La_{0.4}Bi_{0.3}Sr_{0.2}Ba_{0.1}MnO_3$ (T_S = 1000 °C)	130	0.99	1508	−1.68	This work
$La_{0.4}Bi_{0.3}Sr_{0.2}Ba_{0.1}MnO_3$ (T_S = 1100 °C)	126	0.97	1462	−1.62	This work
$La_{0.5}Eu_{0.2}Ba_{0.3}MnO_3$	143	0.99	1659	−1.84	This work
$La_{0.5}Eu_{0.2}Ba_{0.25}\square_{0.05}MnO_3$	145	0.99	1683	−1.87	This work
$La_{0.5}Eu_{0.2}Ba_{0.15}\square_{0.15}MnO_3$	143	0.99	1659	−1.84	This work
$La_{0.8}Na_{0.2}MnO_3$	290	0.99	3366	−3.74	This work
$La_{0.8}Na_{0.1}\square_{10}MnO_3$	264	0.99	3064	−3.40	This work
$La_{0.8}\square_{0.20}MnO_3$	47	0.99	545	−0.60	This work
$Sm_{0.55}Sr_{0.45}MnO_3$	200	0.99	2321	−2.58	This work
$Sm_{0.45}Pr_{0.1}Sr_{0.45}MnO_3$	168	0.99	1949	−2.17	This work
$Sm_{0.35}Pr_{0.2}Sr_{0.45}MnO_3$	173	0.98	2007	−2.23	This work

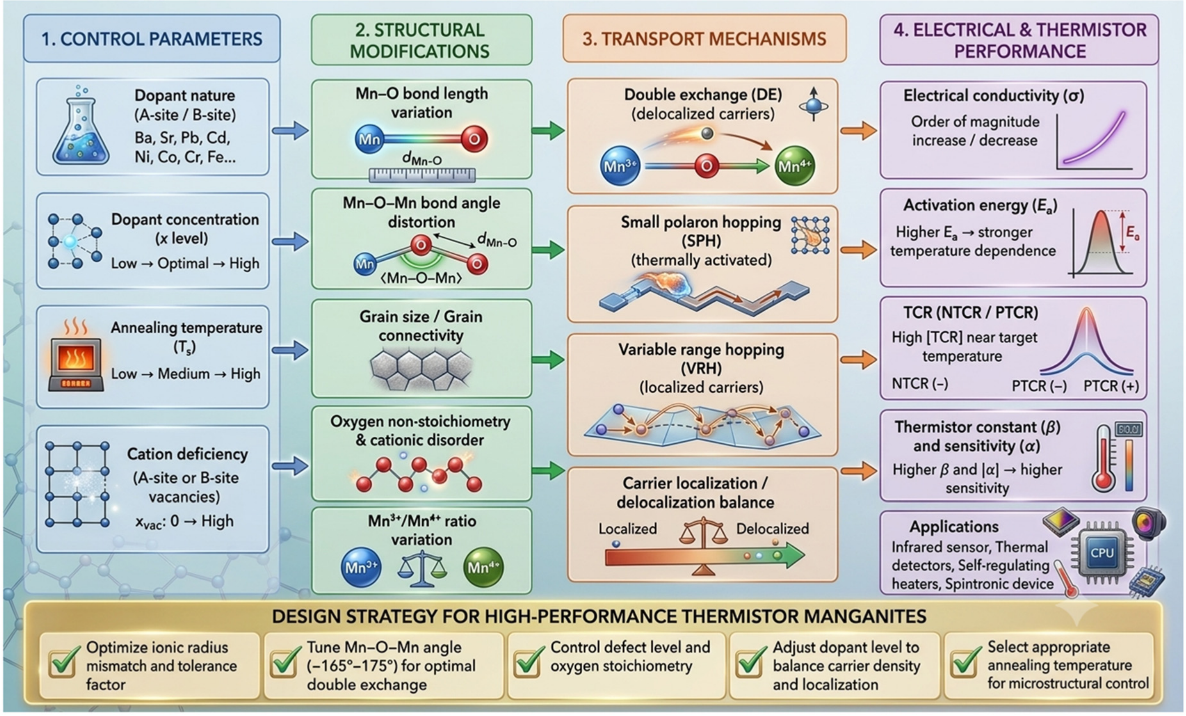

Fig. 18 Comparative schematic overview of the relationships between doping, structural modifications, conduction mechanisms, and thermistor properties in manganites.

(SPH),[13–16] and variable range hopping (VRH). The predominance of one mechanism over another depends strongly on the degree of structural disorder, the carrier concentration, and thermal activation energy. Systems exhibiting strong carrier localization generally display high activation energies and enhanced NTCR responses, whereas compounds with dominant double-exchange interactions tend to exhibit metallic-like conduction and PTCR behavior near the metal–semiconductor transition. From a thermistor-design perspective, the comparative study summarized in Fig. 18 suggests several important guidelines for obtaining high-performance manganite thermistors:

- Optimization of the Mn^{3+}/Mn^{4+} ratio to maximize carrier hopping efficiency while preserving transport stability.
- Careful control of ionic-radius mismatch to tune structural distortion and electronic bandwidth.
- Use of moderate B-site substitution to enhance the NTCR response without excessively suppressing conductivity.
- Optimization of annealing temperature to improve grain connectivity while minimizing excessive carrier localization.
- Controlled cation deficiency engineering to tailor PTCR/NTCR responses and transition temperatures for targeted applications.

The present comparative analysis also highlights several unresolved issues that require further investigation. In particular, the coexistence and competition between double exchange, small polaron hopping, and variable range hopping mechanisms remain difficult to quantify universally across different manganite families. Moreover, the respective contributions of grain boundaries, oxygen non-stoichiometry, and nanoscale structural disorder to the electrical transport properties are still not fully understood. These aspects complicate the establishment of universal predictive models correlating structural parameters with thermistor performance. Nevertheless, the comparative synthesis presented in Fig. 18 demonstrates that manganites constitute a highly versatile platform for thermistor applications due to the remarkable tunability of their transport properties through compositional engineering and processing optimization. The possibility of achieving both large NTCR and PTCR responses over broad temperature ranges makes these materials promising candidates for infrared sensors, thermal detectors, self-regulating devices, and multifunctional electronic systems.

IV. Conclusions

In this work, the electrical transport properties of manganite perovskites have been systematically analyzed by correlating conduction mechanisms, TCR behavior, and thermistor parameters with key controlling factors, namely dopant nature, dopant concentration, annealing temperature, and A-site deficiency. The results demonstrate that electrical conduction arises from a complex interplay between Mott-VRH, Shklovskii–Efros VRH, and small polaron hopping mechanisms, with clear temperature-dependent crossovers. It is shown that the nature of the dopant plays a crucial role in tuning lattice distortion, carrier density, and double exchange interactions, thereby strongly influencing conductivity and activation energy. Increasing dopant concentration modifies the Mn^{3+}/Mn^{4+} ratio and structural parameters, leading to significant shifts in the metal–semiconductor transition and transport behavior. Annealing temperature is identified as a key extrinsic parameter controlling the microstructure, grain connectivity, and defect states, resulting in substantial variations in electrical conductivity and conduction regimes. Furthermore, A-site deficiency emerges as an effective strategy for enhancing electrical performance through the modulation of structural disorder and carrier concentration. The TCR analysis reveals highly tunable NTCR and PTCR responses, with exceptionally high sensitivity values, while the extracted thermistor parameters (E_a, β, and α) exhibit strong correlations, confirming the thermally activated nature of charge transport. Notably, compositions exhibiting high activation energy and β values demonstrate superior thermal sensitivity, making them attractive for thermistor and sensing applications. This study highlights the effectiveness of compositional and processing engineering in tailoring the electrical and thermistor properties of manganites. A comparative analysis of the investigated manganite systems further reveals that high-performance thermistor behavior results from a delicate balance between structural distortion, carrier localization, grain connectivity, and double-exchange interactions. In general, optimized thermistor responses are obtained through controlled tuning of the Mn^{3+}/Mn^{4+} ratio, moderate lattice distortion, appropriate annealing conditions, and carefully engineered cation deficiency. The present study also highlights that the coexistence of multiple transport mechanisms, including double exchange, small polaron hopping, and variable range hopping, remains one of the principal unresolved challenges for establishing universal predictive models correlating structural parameters with thermistor performance. Nevertheless, the proposed comparative framework provides practical design guidelines for the development of advanced manganite-based thermistors with tunable NTCR/PTCR characteristics and enhanced thermal sensitivity. The ability to control conduction mechanisms and thermal sensitivity over a wide range establishes these materials as promising candidates for next-generation thermal sensors, infrared detectors, and multifunctional electronic devices.

Conflicts of interest

The authors declare that they have no known competing financial interests or personal relationships that could have appeared to influence the work reported in this paper.

Data availability

All the data that support this research are included within the article.

References

1 Y. Moualhi and H. Rahmouni, Contribution of multiple trapped centers to the transport properties and scattering processes in perovskite systems, *Comput. Mater. Sci.*, 2025, **246**, 113479.
2 S. H. Jabarov, A. Kh Nabiyeva, E. M. Huseynov, G. T. Imanova, A. V. Trukhanov and S. V. Trukhanov, Dielectric and electrical properties of $La_{0.5}Ba_{0.5}MnO_3$ and $La_{0.97}Ba_{0.03}MnO_3$ perovskites, *J. Porous Mater.*, 2024, 1–6.
3 C. Xia, Z. Li, S. Wang, B. A. Beshiwork and B. Lin, Recent progress on efficient perovskite ceramic anodes for high-performing solid oxide fuel cells, *Int. J. Hydrogen Energy*, 2024, **62**, 331–344.
4 S. M. Yakout, Spintronics: Future Technology for New Data Storage and Communication Devices, *J. Supercond. Novel Magn.*, 2020, **33**, 2557–2580.
5 K. U. P. Okpechi, E. C. Nwaokorongwo and U. Joseph, Physical Properties of Magnetic Materials of Cobalt Oxide, Iron Oxide and Manganese Oxide, *J. Basic Appl. Sci. Res.*, 2024, **2**, 129–134.
6 Y. Moualhi, H. Rahmouni and F. Bahri, Doublet doped titanate ferroelectric system for capacitors and NTC thermistor applications, *Sens. Actuators, A*, 2024, **377**, 115596.
7 A. Ghodhbani, Y. Moualhi, A. Midouni, M. A. Albedah, H. Rahmouni, K. Khirouni and H. Belmabrouk, Tunable electrical transport and conduction pathways in La0.8Ca0.2Mn0.5Cu0.5O3: toward bolometric applications, *Mater. Sci. Eng. B*, 2026, **327**, 119295.
8 Z. Song, Z. Chen, K. Wang and Y. Guo, Sr-Doped YMnO3 NTC Thermistors with Enhanced Stability over a Wide Temperature Range of −150 to 400 °C, *Ceram. Int.*, 2026, **52**(15), 30155–30163.
9 I. Ouni, Y. Moualhi and H. Rahmouni, Regarding application in sensor; a comparative study of electrical properties of Pr0.8X0.2MnO3 (X = Na and X = K) ceramics, *Inorg. Chem. Commun.*, 2025, **179**, 114756.
10 H. R. Jung, S. G. Lee, D. J. Lee and Y. O. Jo, Structural and electrical properties of nickel manganite ceramics for NTC thermistor material, *Sci. Adv. Mater.*, 2017, **9**(8), 1346–1349.
11 P. Biswas, A. Dev, P. Kumar, R. K. Singh and M. Kar, Adequate energy and power density in double-modified (Ag & Al) manganites for supercapacitor and thermistor applications, *J. Power Sources*, 2025, **653**, 237727.
12 X. Dong, H. Han, J. Liu, Y. Bian, X. Ke, N. Chen and J. Chen, Enabling the widely adjustable δTC thermistor functionality in perovskite manganates for temperature range alarming, *J. Am. Ceram. Soc.*, 2025, **108**(10), e70001.
13 N. F. Mott and W. D. Twose, The theory of impurity conduction, *Adv. Phys.*, 1961, **10**, 107–163.
14 Y. Moualhi, H. Rahmouni and K. Khirouni, Usefulness of theoretical approaches and experiential conductivity measurements for understanding manganite-transport mechanisms, *Results Phys.*, 2020, **19**, 103570.
15 N. F. Mott, Electrons in disordered structures, *Adv. Phys.*, 1967, **16**(61), 49.
16 N. F. Mott, Conduction in non-crystalline systems: IV Anderson localization in a disordered lattice, *Philos. Maga.*, 1970, **22**, 7.

17 N. F. Mott, Conduction in glasses containing transition metal ions, *J. Non Cryst. Solids*, 1968, **1**, 1.

18 A. L. Efros and B. I. Shklovskii, Coulomb gap and low temperature conductivity of disordered systems, *J. Phys. C: Solid State Phys.*, 1975, **8**(4), 49.

19 J. B. Goodenough, Direct cation-cation interactions in several oxides, *Phys. Rev. B*, 1960, **117**, 1442.

20 Y. Moualhi, M. A. Alamri, A. Jbeli, N. A. Althumairi, S. El Kossi, R. A. Brahem and H. Rahmouni, Elaboration of La(Sr/Na)Mn(Ti)O_3 ceramic, structural, and morphological investigations, and contribution of direct and indirect interactions on transport properties, *Ceram. Int.*, 2024, **50**(9), 16587–16597.

21 Y. Moualhi, A. Mleiki, H. Rahmouni, K. Khirouni and A. Cheikhrouhou, Temperature, frequency and bias voltage effects on the electrical transport properties of (SmPrSr)MnO_3 perovskite, *Mater. Res. Bull.*, 2022, **155**, 111976.

22 M. Pollak, Approximations for the ac impurity hopping conduction, *Phys. Rev.*, 1964, **133**(2A), A564.

23 K. Ramya, S. Bharadwaj, S. Pola, G. S. Okram and Y. Kalyanalakshmi, Role of divalent doping at A-sites (A = Ca2+, Sr2+, Ba2+ & Pb2+) on thermoelectric and magnetoresistive properties in La0.67(Bi0.0835Na0.0835)A0.165MnO3, *J. Alloys Compd.*, 2025, **1010**, 177464.

24 S. Joseph, R. E. John and K. V. Saban, Unraveling the effects Mn-site doping on structural, magnetic and magnetotransport properties of Nd0.67Sr0.33Mn0.9T0.1O3 (T = Mn, Fe, Cr, Ni), *Ceram. Int.*, 2019, **45**, 21249–21262.

25 Y. Li, H. Zhang, Q. Chen, D. Li, Z. Li and Y. Zhang, Effects of A-site cationic radius and cationic disorder on the electromagnetic properties of La0.7Ca0.3MnO3 ceramic with added Sr, Pb, and Ba, *Ceram. Int.*, 2018, **44**(5), 5378–5384.

26 R. Hanen, A. Mleiki, H. Rahmouni, N. Guermazi, K. Khirouni, E. K. Hlil and A. Cheikhrouhou, Effect of the nature of the dopant element on the physical properties of X-PrCaMnO system (X = Cd, Sr, and Pb), *J. Magn. Magn. Mater.*, 2020, **508**, 166810.

27 Y. Moualhi, R. M'nassri, H. Rahmouni, M. Gassoumi and K. Khirouni, Possibility of controlling the conduction mechanism by choosing a specific doping element in a praseodymium manganite system, *RSC Adv.*, 2020, **10**(56), 33868–33878.

28 P. T. Phong, N. V. Khien, N. V. Dang, D. H. Manh, L. V. Hong and I.-J. Lee, Effect of Pb substitution on structural and electrical transport of $La_{0.7}Ca_{0.3-x}Pb_xMnO_3$ ($0 \le x \le 0.3$) manganites, *Phys. B: Cond. Mater.*, 2015, **466**, 44.

29 D. Y. Cao, Y. Y. Zhang, W. X. Dong, J. Yang, W. Bai, Y. Chen, G. S. Wang, X. L. Dong and X. D. Tang, Structure, magnetic and transport properties of $La_{0.7}Ca_{0.3-x}Sr_xMnO_3$ thin films by sol-gel method, *Ceram. Int.*, 2015, **41**, S381.

30 A. Khatun, P. Aich and D. Topwal, Role of cationic size mismatch and effect of disorder in mixed valent manganites, *AIP Adv.*, 2023, **13**(2), 025125.

31 R. Hanen, Y. Moualhi and H. Rahmouni, Pr0.7Ca0.3Mn0.8-Cr0.2O3 as a promising candidate for sensor and thermistor applications: investigation of TCR, SF, β, and α parameters, *Mater. Adv.*, 2026, **7**, 5171–5182.

32 R. Hanen, Y. Moualhi, A. Selmi and H. Rahmouni, Mott and Jonscher Models for conductance analysis of Chromium-PCMO oxide: thermistor parameters test for thermosensitive applications, *Ceram. Int.*, 2026, **52**, 15681–15691.

33 X. Liang, Z. Wang, Z. Chen, J. Jiang, J. Han, Y. Wang, H. Wang, Z. Pan, J. Sun, J. Ma, X. Jiang, J. Peng, X. Liu and X. Gu, Refined Sr ion ratio to improve room temperature TCR of $La_{1-x}Sr_xMnO_3$ ($0.175 \le x \le 0.235$) polycrystalline ceramics, *J. Mater. Sci.: Mater. Electron.*, 2024, **35**(26), 1–18.

34 L. Vedmid, O. Fedorova, V. Balakireva, S. Uporov, E. Sterkhov and S. Belyakov, Gadolinium manganites substituted with barium $Gd_{1-x}Ba_xMnO_3$ (x = 0.0; 0.15; 0.18; 0.25): Structural transitions, microstructure, magnetic and electrical properties, *J. Alloys Compd.*, 2023, **953**, 170155.

35 Y. Moualhi, R. M'nassri, M. M. Nofal, H. Rahmouni, A. Selmi, M. Gassoumi, N. Chniba-Boudjada, K. Khirouni and A. Cheikrouhou, Influence of Fe doping on physical properties of charge ordered praseodymium–calcium–manganite material, *Eur. Phys. J. Plus*, 2020, **135**, 1–23.

36 Y. Moualhi and H. Rahmouni, Influence of the structural disorder and applied bias voltage variations on the hopping conduction mechanisms, scattering processes, and temperature coefficient of resistance characteristics of Sm0.55_xPr$_x$Sr0.45MnO3 ($0 \le x \le 0.4$) ceramics, *Mater. Chem. Phys.*, 2025, **332**, 130185.

37 I. Belal and F. E. Meriche, Study of the effect of doping and processing conditions on the temperature coefficient of resistivity of perovskite manganite doped at A-site: $A_{1-x}R_xMnO_3$, *Diss*, 2024.

38 B. Udeshi, K. Gadani, K. N. Rathod, H. Boricha, V. G. Shrimali, S. Solanki, A. Zankat, V. S. Vadgama, M. Gal, D. Dhruv, A. D. Joshi, R. K. Trivedi, P. S. Solanki and N. A. Shah, Effect of annealing environments on structural and electrical properties of La0.5Nd0.5MnO3 manganites, *Mater. Chem. Phys.*, 2020, **247**, 122833.

39 Y. Zhou and Z. Xinde, Sh. Li, Effect of heat treatment condition on magnetic, electrical transport and magnetoresistance properties of La0.67Sr0.33MnO3 manganite coatings, *Ceram. Int.*, 2018, **44**(13), 15010–15018.

40 A. Mleiki, A. Khlifi, H. Rahmouni, N. Guermazi, K. Khirouni, E. K. Hlil and A. Cheikhrouhou, Magnetic and dielectric properties of Ba-lacunar La0.5Eu0.2Ba0.3MnO3 manganites synthesized using sol-gel method under different sintering temperatures, *J. Mater. Sci.: Mater. Electron.*, 2020, **502**, 166571.

41 A. Marzouki-Ajmi, H. Omrani, W. Cheikhrouhou-Kouba, M. Koubaa and A. Cheikhrouhou, Effect of barium-deficiency on the structural, magnetic, and magnetocaloric properties of La0.65Ba0.35_x□xMnO3 ($0 \le x \le 0.2$) manganites, *J. Alloys Compd.*, 2017, **690**, 403.

42 R. M'nassri, W. Cheikhrouhou-Koubaa, N. Chniba Boudjada and A. Cheikhrouhou, Effect of barium-deficiency on the structural, magnetic, and magnetocaloric properties of La0.6Sr0.2Ba0.2_x□xMnO3 ($0 \le x \le 0.15$), *J. Appl. Phys.*, 2013, **113**, 073905.

43 A. Mleiki, R. M'nassri, W. Cheikhrouhou-Koubaa, A. Cheikhrouhou and E. K. Hlil, Structural characterization, magnetic, magnetocaloric properties and critical behavior in lacunar La0.5Eu0.2Ba0.2□0.1MnO3 nanoparticles, *J. Alloys Compd.*, 2017, **727**, 1203.

44 Y. Moualhi and H. Rahmouni, Impact of angle and bond distance variation on the transport properties of perovskites, *Phys. B*, 2025, **714**, 417472.

45 H. Y. Hwang, S.-W. Cheong, P. G. Radaelli, M. Marezio and B. Batlogg, Structural effects on the colossal magnetoresistance in perovskite manganites, *Phys. Rev. Lett.*, 1995, **75**, 914–917.

46 R. B. Belser and W. H. Hicklin, Temperature coefficients of resistance of metallic films in the temperature range 25 to 600 °C, *J. Appl. Phys.*, 1959, **30**(3), 313–322.

47 A. Feteira, Negative temperature coefficient resistance (NTCR) ceramic thermistors: an industrial perspective, *J. Am. Ceram. Soc.*, 2009, **92**(5), 967–983.

48 G. Lavenuta, Negative temperature coefficient thermistors, *Sensors*, 1997, **14**(5), 46–55.

49 Z. P. Nenova and T. G. Nenov, Linearization Circuit of the Thermistor Connection, *IEEE Trans. Instrum. Meas.*, 2009, **58**, 441–449.

50 C. Yuan, X. Liu, M. Liang, C. Zhou and H. Wang, Electrical properties of Sr–Bi–Mn–Fe–O thick-film NTC thermistors prepared by screen printing, *Sens. Actuators, A*, 2011, **167**, 291–296.

51 G. M. Gouda and C. L. Nagendra, Structural and electrical properties of mixed oxides of manganese and vanadium: A new semiconductor oxide thermistor material, *Sens. Actuators, A*, 2009, **155**, 263–271.

52 K. Moualhi and M. Annabi, Mouldi Zouaoui, Multifunctional Behavior of GdCa$_2$Cu$_3$O$_\delta$ for Capacitor and Thermistor Applications, *J. Am. Ceram. Soc.*, 2026, **109**(5), e70799.

53 V. K. Haripriya, A. George and K. A. Malini, Effect of Synthesis Route on the Structural and Electrical Properties of Co Substituted Ni-Mn Oxide Based NTC Thermistors, *Curr. Appl. Phys.*, 2026, **84**, 88–96.

54 T. Reimann and J. Töpfer, Low-temperature sintered Ni–Zn–Co–Mn–O spinel oxide ceramics for multilayer NTC thermistors, *J. Mater. Sci.: Mater. Electron.*, 2021, **32**(8), 10761–10768.

55 K. Samatha and R. Sagar, High specific capacitance and NTC behavior of substituted cobalt oxide spinels for electrochemical supercapacitor and thermistor applications, *Inorg. Chem. Commun.*, 2024, **160**, 112017.

56 V. K. Haripriya, A. George and K. A. Malini, Influence of Cobalt Substitution on the Structural and Electrical Properties of NiMn$_2$O$_4$-Based NTC Thermistors, *Results Surf. Interfaces*, 2026, 100781.

57 I. Ouni, Y. Moualhi and H. Rahmouni, Thermistor and capacitor parameter analysis through electrical and dielectric investigations of manganite systems for technological applications, *Sens. Actuators, A*, 2025, **384**, 116300.

58 A. Ghodhbani, Y. Moualhi, W. Dimassi, R. M'nassri, H. Rahmouni and K. Khirouni, Contribution of strong electron-phonon interaction in the transport properties of La0.8Ca0.2Mn0.5Ni0.5O3 system, *Phys. B*, 2024, **683**, 415964.